PARAMETER ESTIMATION OF NETWORK STRUCTURES WITH APPLICATION TO VASCULAR NETWORKS

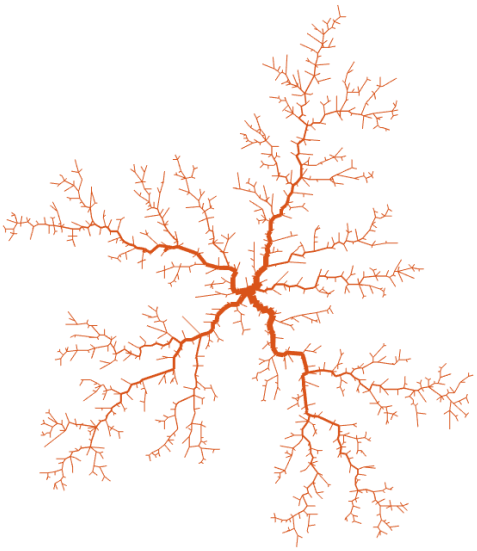

Jenny Espelund Hognestad

Master thesis in Applied and Computational mathematics

Department of Mathematics, University of Bergen

November 21, 2022

Acknowledgements

First of all I will direct my biggest gratitude towars my supervisors, Jan Martin Nordbotten and Erlend Hodneland. Thank you, Jan, for always standing steady at the helm and for pointing out the direction so clearly. I have really appreciated all the help you provided in such an inspiring way, and for your apparent ability to understand my exact question even when I don't. Thank you, Erlend, for always having an open door and time for "just one more thing". Your expertise within this field and the interest you have shown for this work have been a great source of help and motivation. I am so grateful for all the thorough explanations as well as nifty tips and tricks you have provided.

Further, I must thank everyone who also contributed to this thesis in one way or another. Huge thanks to Otilie for the drawing, and to Jessica for proofreading. To those of you who helped me with coding issues and who lent me their textbooks. I am also very grateful for being so warmly included by everyone at MMIV this fall.

No thesis could have been written without any breaks, and I thank everyone who made me think about other things than blood vessels this year. Hugs are sent to co-students, Tirsdagsklubben and everyone who shared shared lunches, breaks, laughs, frustrations and waffles with me at Realfagbygget and Haraldsplass. And last, but not least, thanks to all my outside-of-school friends, my beloved roomies and my family for always being there when I need it.

Abstract

Background: The complex and hierarchical structure of the vascular system constitutes a main challenge in blood flow modelling, to which multiscale modelling has been a common approach. Recent publications suggest to represent large vessels as a graph structure with Hagen-Poiseuille flow in graph edges, and the intricate mesh of microscale capillaries as a porous medium with Darcy flow. However, a coupling between scales that is both mathematically and physiologically sound remains a challenge. Due to limited resolution in medical imaging devices, there is a large number of vessels below the scale of pixel size whose structure is unknown. Hence, we can only make structural and modeling assumptions about the flow distribution from macroscale to microscale vessels.

Methods: In this thesis, we have investigated whether a complex network may be replaced by a simplified, coarse model with a fewer model parameters, hoping to eliminate the need to know the exact mesoscale network structure. In this respect, we estimated a set of transfer conductivity parameters on three different graph structures. A coarse network approximation based on the estimated transfer conductivity was used in an idealized model for arterial flow in brain, and compared with a reference model where the mesoscale network was represented as a graph model.

Results: The transfer conductivity decreased with radial distance R from the source node when the flow path length was associated with R. For the coarse model, we found the error to be small for all three graph structures given small pressure gradients in the porous domain. We also found the transfer conductivity to be highly dependent on the conductivity of single graph edges.

Conclusions: Our study confirms modeling assumptions about the flow distribution being dependent on radial distance from the source node. However, the exact functional relationship will depend on the network structure. Moreover, since a significant portion of the pressure drop in the brain vasculature is over the arterioles and venules, and not in the capillaries, we claim that our coarse model can be sufficiently accurate for modelling purposes. Finally, the single graph edge influence on transfer conductivity suggests that a coarse model in the context of parameter estimation may be used for diagnostic purposes, as several medical conditions involve changes in brain vascular microstructure.

Contents

List of symbols

A	area	m^2
g	gravitational acceleration	ms^{-2}
h	hydraulic head	m
k	permeability	m^2
K^D	Darcy conductivity	$m^2 s^{-1} Pa^{-1}$
K^N	network conductivity	$m^3 s^{-1} Pa^{-1}$
K^T	transfer conductivity	$s^{-1} Pa^{-1}$
L	characteristic linear dimension	
L_m	graph level	
l	tube/edge length	m
M	maximum graph level	
p	fluid pressure	Pa
p^D	Darcy pressure potential	Pa
p^N	network pressure potential	Pa
q	volumetric flux	$m^3 s^{-1} m^{-2}$
q^D	Darcy flux	$m^3 s^{-1} m^{-2}$
q^N	network flux	$m^3 s^{-1}$
q^T	transfer flux	$m^3 s^{-1} m^{-3}$
r	tube/edge radius	m
r^D	source/sink term	$m^3 s^{-1} m^{-3}$
r_R	root edge radius	m
r_T	terminal edge radius	m
Re	Reynolds number	
$\mathbf{u}$	fluid velocity vector	ms^{-1}
v_n	outward normal vector	
z	elevation above datum	m
α_r	radius reduction factor	
α_l	length reduction factor	
ϕ	material porosity	
κ	hydraulic conductivity	ms^{-1}
μ	fluid viscosity	$Pa \cdot s$
ω	distribution area	
Ω	domain	
ρ	fluid density	kgm^{-3}
θ	rotation angle	
$\mathscr{E}$	edges	
$\mathscr{E}_i$	edges meeting in node i	
$\mathscr{G}$	graph	
$\mathscr{G}'$	subgraph	
$\mathscr{N}$	nodes	
$\mathscr{N}_I$	interior nodes	
$\mathscr{N}_R$	root node	
$\mathscr{N}_T$	terminal nodes	

$\mathscr{N}_{T'}$	sub graph terminal nodes	
$\mathscr{N}_i$	neighbours of node i	
$\mathscr{T}$	rooted tree	
$\nabla\cdot$	divergence operator	m^{-1}
∇	gradient operator	m^{-1}
Δ	Laplacian operator	m^{-2}

1 Introduction

Many biological transport systems, such as the branches and roots of trees, but also the arteries and veins in the human body, form network structures where flow is driven by pressure gradients. In this thesis we investigate mathematical modelling of such systems, where we aim to understand the connection between discrete network structures and a coarse network approximation. The considered field of application is the modelling of brain hemodynamics. Within this field, such a coarse, network approximating model has been proposed as a remedy to the lack of information about the blood vessel network in the brain.

Robust and accurate mathematical models may serve as important clinical tools to understand and predict flow patterns and transport mechanisms in the brain vasculature. As many severe medical conditions are linked to disruptions in the microvascular circulation, improved measurements and understanding of the flow dynamics can contribute to better diagnostics, treatments and surgical planning. For instance, changes in capillary perfusion has been detected in brain cancer survivors, to which more precise, patient-specific estimates are wanted in order to assess treatment response and sequela (Troudi et al., 2022). Microvascular alterations are also seen in stroke patients (Rubin et al., 2000) and in relation to Alzheimer's disease (Chen et al., 2011) as a result of occlusion in capillary vessels. Modern imaging technology such as magnetic resonance imaging (MRI) and computerized tomography (CT) have revolutionized the field of diagnostics and treatment, as it allows for in vivo investigations of anatomical and dynamic responses in organ tissue through both qualitative and quantitative image acquisitions. For instance, through dynamic contrast-enhanced (DCE) MRI, parametric maps of biomarkers may be dervied from time-intensity curves of contrast agent concentration in brain tissue, as the variation in concentration intensities depends on vessel network properties (Gordon et al., 2014). More generally, modern imaging technology combined with mathematical models may provide parameter estimations both useful for diagnostic purposes as well as for simulations predicting e.g. surgical outcomes (Voß et al., 2016).

The vascular system in the human body forms a huge and complex network composed of vessels at different spatial scales, ranging from the aorta with radius $\sim$1 to 2 centimeters (Greenfield & Patel, 1962) to the capillaries on a few micrometers (Perdikaris et al., 2016). Due to the size, complexity and large variations in spatial scales, the main modelling challenge is to accurately model and connect flow at different scales without too high a computational cost. Multi-scale models have become a common approach to this challenge, and involves combining two or more well known models accounting for flow at different scales to constitute a global flow model. For instance, in Hodneland et al. (2019) and Koch et al. (2020), macroscale vessels are modeled as a 1D graph with Hagen-Poiseuille flow in graph edges, while the capillary bed is considered as a 3D porous domain and microcirculation is modeled with Darcy's law. In these models, structure details such as vessel wall elasticity and vessel curvature, as well as the non-linear and non-Newtonian behaviour of blood flow is disregarded. However, these

are simplifications that one are aware of and thereby can account and even correct for. For instance, in Qohar et al. (2021), the non-linear effects due to pressure drop at vessel junctions and vessel elasticity is included in the model. Yet, what remains a challenge due to *unknown* features is the coupling between the vessels at macro and micro scale. Due to limited image resolution, the structure of the vessel network is unknown at spatial scales below image resolution, meaning that the mesoscale network constitutes a gap between the visible macroscale network and the microscale capillary bed that forms a remaining puzzle piece in a complete vascular network model, see Figure 1.1 for illustration. To avoid singularities in the domain, the above referenced models uses spatially distributing functions coupling the 1D graph to the 3D domain through the terminal nodes of the graph. These functions are chosen based on the assumption that the blood distribution is a decreasing function of the distance from the feeding artery. A recently developed model from Hodneland et al. (2021) suggests a different approach: instead of an assumed distribution being given, the mesoscale network is assigned a transfer conductivity, and the flow transferring from macro to micro scale is calculated. The remaining question is then whether there in reality is possible to replace the complex mesoscale network with a set of parameters to obtain a valid, coarse network approximation. This question forms the main objective for this thesis, and will be attempted answered by calculating the transfer conductivity on a set of synthetic networks assumed to share common properties with vessel networks. We also investigate the hypothesis of a spatial dependency on the transferring flow, and test the sensitivity of the transfer conductivity to various network parameters.

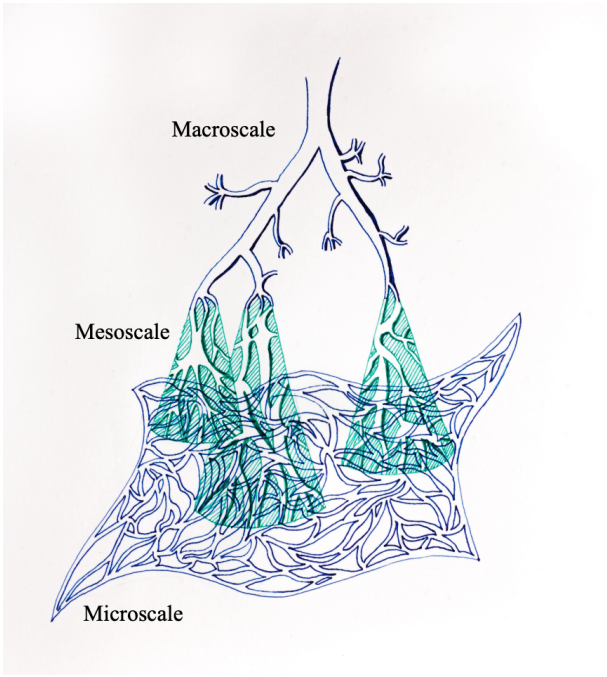

Figure 1.1: *This drawing illustrates the model problem considered in this thesis, and is inspired from the Figure 2 in Hodneland et al. (2021). Only vessels above the spatial scale of a image pixel size (macroscale) are visible in imaging pictures, thus, a flow approximation (green cones) is made between these vessels and the microscale capillary mesh which is considered as a porous medium. Note that the spatial scaling is not realistic, as the microscale vessels are of order* 10^3 *smaller than the macroscale vessels.*

1.1 Contributions

We have generated three different network structures in order to investigate the validity of a coarse network approximation in terms of a transfer conductivity parameter, as proposed in Hodneland et al. (2021). By plotting the transfer conductivity as a function of the radial distance R from the source node, we have confirmed that the assumption of a radial dependent flow distribution holds when there is a correspondence between flow path length and radial distance. This implies that a significant portion of blood flow may be restricted to a support area around the source node, which simplifies the model considerably as it eliminates the need for a full network-domain connectivity. The estimated transfer conductivity as a function of radial distance R from the source node can be found online (https://github.com/rix004/Master). The main contribution of this thesis is the demonstration that a coarse network approximation in terms of the transfer conductivity is valid for an idealized arterial flow model for the brain, given small pressure gradients in the porous domain (capillaries). Since the highest pressure drop in the brain vasculature is over the arterioles and venules, this suggests that our coarse model may be valid, and encourages to further work towards an application to brain vasculature. Finally, we have demonstrated that the transfer conductivity is highly dependent on the radii of single graph edges, indicating that changes in network structure will affect the parameter values. This suggests that estimating the transfer conductivity in patients may have a clinical value in the context of diagnostics, as several medical conditions alters the morphology of the vascular network.

1.2 Thesis outline

Chapter 1 is this chapter and presents the motivation, context and contributions of this thesis.

Chapter 2 provides the reader with the background theory on which the modelling framework is built upon. It includes a brief introduction to the vascular system before the flow equations are presented. We show the derivation of the Hagen-Poiseuille equation from the incompressible Navier-Stokes equations and give a short introduction to basic porous media theory, including Darcy's law. The last section is devoted to traditions and earlier work within the field of blood flow modelling.

Chapter 3 presents the continuous formulation of the two idealized flow models for arterial blood flow used herein. We have implemented one model which will be referred to as the *reference model* to use as reference to the *coarse model*, where we will use a coarse approximation of the mesoscale network.

Chapter 4 includes the methods for the generation of the three different network structures used to model the mesoscale network, as well as the implementation of flow equations for the two different models. It also includes the description of the set-up for code verification.

Chapter 5 presents the numerical results. We start by showing the verification results before presenting

the results on the structured tree, which are also used to validate the code as well as to provide understanding and insight about important parameters. At last we present the results on the unstructured networks, which are considered as the "biological" test cases. A short summary of the main results is listed in the last section.

In **Chapter 6**, the results are discussed and conclusions are drawn. We consider the results in light of an application to brain vasculature and provide suggestions to further work, including a brief consideration about other fields of application.

2 Background theory

In this chapter we present the basic theory to provide context and understanding about the mathematical models used herein. The chapter is structured as follows:

Section 2.1 gives a short presentation of the full vascular system. The aim of this chapter is to provide the reader with sufficient background knowledge about the terminology and function of the system to follow the rest of the chapters. The theory is based on Keener and Sneyd (2009) unless otherwise stated.

In Section 2.2 we show the derivation of the Hagen-Poiseuille equation from the Navier-Stokes equations. The equation is an idealized model for flow in tubes, and will be used to model blood flow in fully resolved vessels in our model. The chapter provides insight about some of the simplifications such an idealization implies.

Section 2.3 is about porous media, some of their properties and flow modelling in this regime. We introduce the concept of a Representative Elementary Volume (REV) and discuss important properties in the context of this thesis. At last we present Darcy's law and the assumptions we do in order to include it in our model.

Finally, in Section 2.4, we go more into detail about modelling of biological networks. At last we look at how it has been attempted to derive mathematical design principles for vascular structure generation through two different approaches: Models based on optimal principles and fractal models.

2.1 The vascular system

The vascular system is the collection of all blood vessels in the body. It is a transport system whose main task is to carry oxygen from the lungs to the body tissues, and carbon dioxide from the tissues back to the lungs. We can think of the vascular system as a loop for the blood flow, starting and ending at the heart. The vessels that transports blood *from* the heart *to* to the tissues are called the *systemic arteries*. From the left heart chamber, the oxygenated blood is pumped into the main artery, which is the largest vessel in the vascular system, named aorta. The aorta can be though of as the main stem in an arterial vessel tree, branching into progressively smaller arteries and even smaller arterioles in order to reach out to all body parts. Finally, the blood reaches the capillaries, which is the vessels that participate in the exchange of gases and nutrients from blood to tissue. The capillaries do not have the same branching structure as the other vessels, but a mesh-like, space filling structure, as their main task is not effective transport over distances, but to effectively deliver oxygen to surrounding tissue (Lorthois & Cassot, 2010). Figure

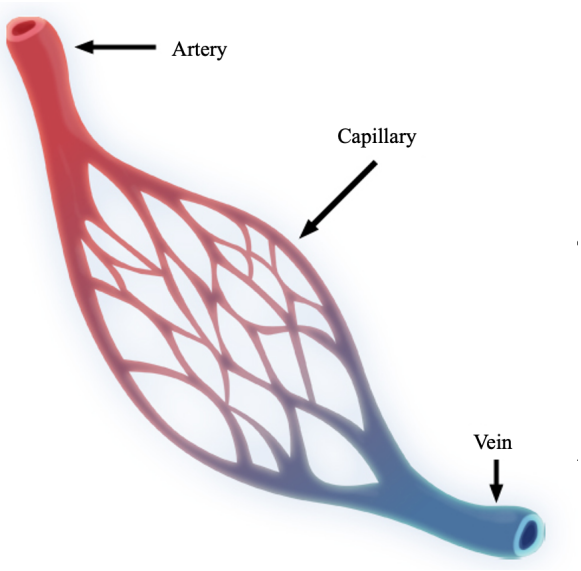

Figure 2.1: *A sketch of a capillary. Note the mesh-like structure and the difference in radii between capillary vessels and the feeding artery and draining vein. The image is reproduced from https://commons.wikimedia.org/wiki/File:Capillary_system_CERT.jpg.*

2.1 illustrate the structure as well as the scale differences between capillary vessels and the arteries and veins. The exchange processes in the capillaries also involves receiving carbon dioxide from the tissue to the blood, which is then transported back to the lungs through the *systemic veins*. Leaving the capillaries, the blood first enters the venules, which progressively widen and join into larger veins before finally converging to the venae cavae. This is the main stem of the venous tree which delivers the carbon dioxide rich blood to the right heart chamber. A similar transport system is found between the heart and the lungs. From the right heart, the carbon dioxide rich blood is pumped into the *pulmonary arterial tree*. The exchange of gases from and to the lungs takes place in the pulmonary capillaries, and as the oxygen rich blood is transported to the left heart chamber through the *pulmonary venous tree*, the loop is closed.

2.2 Idealized flow in tubes

Flow through a cylindrical tube with constant cross-section is a situation where an exact solution can be derived for the Navier-Stokes equations for fluid motion. The solution is the Hagen-Poiseuille equation, named after the german civil engineer Gotthilf H. L. Hagen and the french physiologist Jean L. M. Poiseuille, who independently discovered the relationship experimentally. For Poiseuille, the underlying motivation for the experiments was to understand blood flow in human vasculature. With the right assumptions and simplifications, the relationship is still, after later discoveries of the behavior of blood cells, considered as an acceptable model for this purpose (Sutera & Skalak, 1993).

2.2.1 Laminar flow

The Navier-Stokes equation describing motion of a viscous fluid is given by

$$\rho(\frac{\partial \mathbf{u}}{\partial t} + \mathbf{u} \cdot \nabla \mathbf{u}) = -\nabla p + \mu \nabla^2 \mathbf{u} + \rho \mathbf{g} \tag{2.1}$$

Here, $\mathbf{u}$ denotes the fluid velocity vector, p the fluid pressure, ρ the fluid density, μ the dynamic viscosity of the fluid and $\mathbf{g}$ the gravitational acceleration vector. Equation (2.1) is Newtons second law for viscous fluid motion, where the left hand side is mass times acceleration, and the right hand side is the total force acting on the fluid. The relation

$$Re = \frac{\rho u L}{\mu} \tag{2.2}$$

is called Reynolds number, and is an important, dimensionless quantity in fluid mechanics. Here, u is the flow speed, which can be taken as a spatial average of $\mathbf{u}$ (Huinink et al., 2016), and L is a characteristic linear dimension depending on the tube radius (Formaggia et al., 2010). Reynolds number is a ratio of inertial forces to viscous forces in the fluid, and gives information about the flow behaviour: At relatively high speeds and thus high Reynolds numbers, we have *turbulent* flow. Here, the streamlines of the flow are mixed together, and they are often characterized by swirls. The contrary is *laminar* flow, where the streamlines do not mix, but follows well-defined paths and lies in layers like sheets. The dividing line between turbulent and laminar flow lies at $Re \sim 2000$ to 3000 (Kundu et al., 2015). In the case of laminar flow with $Re < 2000$, Equation (2.1) simplifies considerably as we can neglect the acceleration term on the left hand side to obtain

$$-\nabla p + \mu \nabla^2 \mathbf{u} + \rho \mathbf{g} = 0 \tag{2.3}$$

Without the non-linear term present, exact solutions can be derived with the appropriate choice of boundary conditions and additional assumptions of the flow behaviour.

2.2.2 The Hagen-Poiseuille equation

We consider steady (constant velocity) and fully developed (far from an open end) flow in a narrow, circular tube with radius r, see Figure 2.2. We employ cylindrical coordinates $\mathbf{u} = \mathbf{u}(R, \phi, x)$, and let the x-axis coincide with the tube axis. In this coordinate system we have (Adams & Essex, 2013)

$$\nabla^2 \mathbf{u} = \frac{1}{R}\frac{\partial}{\partial R}(R\frac{\partial u}{\partial R}) + \frac{1}{R^2}\frac{\partial^2 u}{\partial R^2} + \frac{\partial^2 u}{\partial x^2} \tag{2.4}$$

Since the flow is laminar, we assume it to follow more or less straight paths along the x-axis. The only non-zero component of $\mathbf{u}$ is therefore the one in the x-direction, and we are left with only the first term in Equation (2.4). Since the flow is also steady, this component is only dependent of R, so $\mathbf{u} = (0, 0, u(R))$. If we in addition assume constant fluid density so that the gravitation term can be neglected (Kundu

et al., 2015, p. 152), Equation (2.3) reduces to

$$-\frac{dp}{dx}+\mu\frac{1}{R}\frac{d}{dR}(R\frac{du}{dR})=0. \tag{2.5}$$

Since p is only a function of x and u only a function of R, both terms in Equation (2.5) must be constant to sum to zero. The pressure thus falls linearly along the length of the tube in the flow direction. Solving for $u(R)$ by integrating twice we get

$$u(R)=\frac{R^2}{4\mu}\frac{dp}{dx}+C_1 ln(R)+C_2,$$

and by employing no-slip boundary conditions, $u=0$ at $R=r$, we see that we must have $C_1=0$ and $C_2=-\frac{r^2}{4\mu}\frac{dp}{dx}$. Thus

$$u(R)=\frac{R^2-r^2}{4\mu}\frac{dp}{dx}.$$

Finally, we integrate the velocity distribution over the cross sectional area to find the volume flow rate:

$$q=\int_0^r u(R)2\pi R dR=-\frac{\pi r^4}{8\mu}\frac{dp}{dx}. \tag{2.6}$$

This is the Hagen-Poiseuille equation. $\frac{dp}{dx}$ is often approximated over the tube length l as $-\frac{\Delta p}{l}$. Thus we end up with

$$q=\frac{\pi r^4}{8\mu l}\Delta p. \tag{2.7}$$

Worth noticing is the forth power on r, making the flow rate very sensitive to changes in the tube radius.

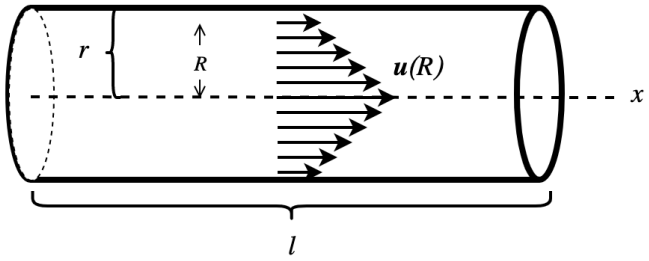

Figure 2.2: *Cylindrical tube with radius r and length l, where the fluid velocity vector* $\boldsymbol{u}$ *depends on the radial coordinate R only.*

2.3 Flow in porous media

2.3.1 Porous materials

A porous medium is any material consisting of a solid matrix and containing pores (Huinink et al., 2016). Rocks, soil and sandbeds as well as wood, skin and biological tissue are just a few examples of materials fitting in to this categorization. Naturally, the structure in these materials are very different from each other. Soil is a porous material because it consists of unconsolidated particles, so the pores are simply the highly unordered void space between the grains. Wood and biological tissue have a perhaps more intuitive distinction between the solid matrix and pores, because the pores are vessels that are meant to transport fluid. However, the same tools for calculations apply to all porous materials, but we need to assign specific values for the properties of the material of interest.

Some of the properties we are concerned about in a porous medium, such as porosity, permeability and saturation of fluid, cannot be considered at a specific point in space. Doing that, we will either be looking at a point within a pore or within the solid part, but the properties of interest are about the relationship between the two. Instead we use the concept of a representative elementary volume (REV). The REV can be thought of as a cut out box or sphere of the porous medium, see Figure 2.3. The REV must be large enough to account for inhomogenities in the medium and allow for meaningful averages to be defined (Nordbotten & Celia, 2011), but also small enough to say something meaningful about spatial variations. Properties of the medium can then be assigned to each point in space based on the REV surrounding that point, and continuous formulations can still describe changes within the medium.

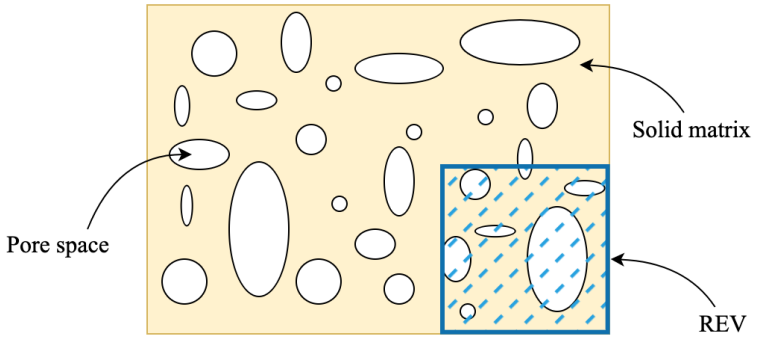

Figure 2.3: *Illustration of a cross-section of a porous medium and a Representative Elementary Volume (REV).*

The specific permeability k is an important characteristic of a porous medium. It provides information about how the geometry of the pore space in the medium contributes in the conductivity, i.e., it indicates how much resistance the fluid experiences due to the material itself when flowing through it (Dullien,

1979). The resistance is due to friction in the fluid-material interface, and will therefore increase as the internal surface area in the pores increases (Huinink et al., 2016). There are two factors that hence determine the value of k: The porosity of the material and the pore radii. Porosity is the ratio of void space to the total volume of material, and as the porosity decreases, the internal surface area will increase, which results in higher resistance and lower permeability. The pore radii affects the resistance in that smaller radii gives a bigger internal surface area, and hence bigger resistance and lower permeability. An important flow feature is that fluid will always search for the flow paths with the lowest resistance. Considering an idealized pore throat as a cylindrical tube, we recall from the Hagen-Poiseuille equation that the flow in a pore throat is extremely dependent on the pore radius. This will often result in flow paths dominated by bigger pores, while other, very small pores are hardly engaged in the flow. For a given flow path, it will therefore be the pore with the lowest radius engaged in the flow that determines the path resistance (Huinink et al., 2016).

2.3.2 Darcy's law

The pore space in a porous medium as usually highly geometrically complex with large variations in both pore radii and lengths. This makes flow calculations on a pore scale cumbersome or even impossible in a large pore network, as it requires knowledge about characteristics of the medium that might be difficult to extract. Calculations on flow in porous media is therefore usually done in a macroscopic manner by considering properties at REV scale and by looking at the filtration velocity rather than the fluid velocity within the pores. The fluid and material properties that indicates how easily the fluid flows through the material are usually collected in the hydraulic conductivity parameter κ, reading

$$\kappa = \frac{k\rho g}{\mu}, \tag{2.8}$$

where k is the permeability of the porous medium, ρ is the fluid pressure, g is the gravitational acceleration and μ is the viscosity of the fluid. The equation that relates the properties of a porous medium to the macroscopic flow rate q^D is the famous Darcy's law (Darcy, 1856), which reads

$$q^D = -\kappa \nabla h \tag{2.9}$$

where

$$h = \frac{p}{\rho g} + z \tag{2.10}$$

is often referred to as the hydraulic head, describing the mechanical energy state of the system. The first term is the pressure head, which is the fluid pressure p scaled by the fluid density and the gravitational acceleration. The second term is the elevation head, and is simply the elevation z of the measuring point above some datum.

It is important to notice that the volumetric flux q^D is *not* the velocity of the fluid within the pores,

which we recall may be highly heterogeneous, but rather the volume of fluid per time per *total* area, including both the pores and the solid matrix. If we assume that all material and fluid properties as well as the gravitational acceleration are scalars, we can rewrite Equation (2.9) as

$$q^D = \frac{k}{\mu}(\nabla p + \rho g \nabla z) \tag{2.11}$$

In this thesis, Darcy's law will be used to model microcirculation in the capillaries, and we assume that the differences in elevation is negligible. Thus, we follow the assumption about blood flow being driven solely by pressure gradients (Keener & Sneyd, 2009), which means that the last term in the parenthesis in Equation (2.11) can be neglected, and we are left with

$$q^D = -K^D \nabla p \tag{2.12}$$

where

$$K^D := \frac{k}{\mu} \tag{2.13}$$

2.4 Modelling of hemodynamics and vascular network structure

Due to varying structure and spatial scales in vasculature, the flow behaviour of blood changes during circulation. In the largest macroscale vessels the flow is nearly turbulent, but becomes laminar at lower scales as resistance increases with smaller radii (Formaggia et al., 2010). In addition, the presence of blood cells makes the viscosity depend on the vessel radii. Blood is primarily composed of red and white blood cells and $\sim 55\%$ plasma which mainly contains water ($\sim 92\%$) (Formaggia et al., 2010). When the vessels narrow and approach a critical limit ~ 1 mm, the red blood cells will move to the center of the vessel, while the plasma stays in contact with the vessel wall and promotes the cell movement (Formaggia et al., 2010). This results in a sharp decrease in the apparent fluid viscosity, and is known as the Fåhareus-Lindquist effect (Fåhræus & Lindqvist, 1931). Formaggia et al. (2010) therefore argue that a Newtonian model, where one neglects the viscoelastic effects of blood flow, is acceptable at larger scales or in models where detailed flow behavior is not the main focus.

Flow at macro scale is understood up to a point where sufficiently accurate, patient-specific models are obtained using medical imaging tools to detect the vascular network structure (Perdikaris et al., 2016). Flow dynamics it governed by the unsteady, incompressible Navier-Stokes equations coupled with a model for the flow-structure interactions (Formaggia et al., 2010), but 1D models are considered sufficient for computations of pressure and flow distributions in cases where detailed flow behavior is not important (Perdikaris et al., 2016). 1D approximations involves to take advantage of the cylindrical symmetry of the vessels and often also to assume laminar and steady flow, hence, the vessels can be modelled as a network of cylindrical tubes using the Hagen-Poiseuille equation. Within the field of porous media, this idealized model applied to extremely complex pore spaces has proved to be not only valid, but also useful. This was first demonstrated by Fatt (1956), and has been used to predict important

parameters for flow in porous media, especially multi phase flow (Blunt et al., 2002). Despite the many differences between the pore space in a rock and the blood vessel network, one can argue that the success of network modelling of highly geometrically complex porous material speaks for the validity of such an idealization.

As the smallest capillary vessels have diameters the size of a blood cell, plasma and cells flows with different rates, and the flow in this regime should be considered as multi-phase flow of particles and plasma on a fully resolved scale (Formaggia et al., 2010). However, a common approach in multiscale modelling is to represent the capillary flow in an averaged manner as flow in a porous medium, advantaging its mesh-like structure. Thus, through a coupling with a 1D model of the macroscale vessels, this may constitute an effective discrete-continuous flow model where variations in the bigger arteries can be described vessel-wise, while effects of microvascular diseases can be investigated by varying local parameters like porosity and permeability in the capillary bed (Cookson et al., 2014). Yet, this is provided a reasonable modelling of the mesoscale network forming a coupling between the two.

The representation of the mesoscale vessel network remains a modelling issue. In mixed discrete-continuous models such as Shipley et al. (2019), Hodneland et al. (2019), Koch et al. (2020) and Qohar et al. (2021), the dimensional gap is filled using spatially distribution functions where outflow from terminal nodes are seen as local sources in the continuous domain, which are distributed in a support area around the source point. The distribution is assumed to have a spatial dependence in the sense that more flow is distributed in areas near the source node. Hodneland et al. (2021) suggests a different approach, where the transferring mesoscale flow is calculated using a given *transfer conductivity* between the terminal nodes and the capillary bed. However, such a network conductivity for the mesoscale network is to this date not assessed, and should be approximated on a realistic vessel network to be used in a model.

2.4.1 Approaches to computational vascular structure generation

Simulation of blood flow on computationally generated graph structures may be useful for estimating unknown modelling parameters, provided that the graph is a realistic vasculature representation. Using available information about real network structure, many authors have searched for a set of design principles that may provide understanding about the non-available information. The two main approaches to synthetic network generating algorithms are optimization principles and fractal models (Schreiner et al., 2006). The optimization approach involves to implement theoretical laws for vessel branching derived from physiological principles, often involving the minimization of a cost function (Talou et al., 2021). Such physiologically grounded branching laws have been studied for many years (C. D. Murray, 1926; Kamiya and Togawa, 1972; Zamir, 1976), and are employed in e.g. the Constrained Constructive Optimization (CCO) algorithm as a branching guiding line in the generation of a space-filling, synthetic network within a given domain (Talou et al., 2021). The fractal modelling approach is based on the idea that the structure of the vessel network repeats itself at progressively smaller scales (J. D. Murray, 2002). The many fractal appearing patterns arising in nature have been elucidated by e.g. Mandelbrot (1977),

and owing to its branching and hierarchical structure, the vascular system has been scrutinized in search for fractal properties (Zamir, 1999; Masters, 2004), without any consensus emerging, however (Lorthois & Cassot, 2010).

One particular class of fractal structures arising in several natural growth patterns are Laplacian fractals. These are structures arising from a clustering growth phenomenon governed by the Laplace equation, where the growth is limited by the diffusion to the cluster (Masters, 2004). It has been suggested that vessel formation (angiogenesis) is characterized by such a mechanism. One of the main stages in angiogenesis is the vascular endothelial growth factor (VEGF), which is a process where endothelial cells clusters to form new vascular structures (Martino et al., 2015). Fleury and Schwartz (1999) propose that sheer stresses within a Laplacian pressure field in the endothelial walls is the driving force of the clustering, and hence that diffusion limited aggregation may be used to model angiogenesis . This hypothesis is adopted in Lorthois and Cassot (2010), who argue that healthy vasculature in the brain should be regarded as a fractal, tree-like structure emerging from a Laplacian growth mechanism at larger scales, and the microscale capillary bed as a non-fractal, mesh-like composition.

3 Idealized model for vascular network flow

This chapter outlines the mathematical models used in this thesis. The aim is to investigate a set of parameters defining a unknown, mesoscale vessel network, and to describe this network, we will use a 1D graph with nodes representing the vessel bifurcation points, and edges representing vessel segments. Further, we will compare two different multiscale models representing a network of vessels from macroscale to microscale in the brain. Both models are a composition of a discrete network modelling the visible arteries and a 3D/2D porous medium domain representing the capillaries. The difference in the two models is the representation of the mesoscale network. In the the *reference model*, we use a graph for both the macroscale and mesoscale network, and we couple the graph to the domain directly through its terminal nodes. In the *coarse model*, we use the mesoscale graph to obtain a description of the network conductivity K^T. This parameter is then used to replace the graph by a continuous, linear model for the flow transferring from the terminal nodes of the macroscale network to the domain, as proposed in Hodneland et al. (2021). Our model involves several simplifications. By employing the Hagen-Poiseuille flow model we consider vessels as static, straight and cylindrical tubes with constant cross section, hence, elasticity in vessel walls is ignored, as well as the non-linear flow behaviour. We consider blood as a Newtonian fluid with constant density and viscosity. We also assume all capillaries to have equal and constant radius when regarding the capillary bed as homogeneous and isotropic with constant permeability.

In Section 3.1, the geometry and terminology of the graph representing the discrete vessel network is presented. Then the governing equations common for both models are presented in Section 3.2, while equations concerning the coupling in the reference and the coarse model is presented in Section 3.3 and Section 3.4, respectively.

3.1 Geometry of the discrete vessel network

The vessel network is modeled as a graph $\mathscr{G}$ consisting of a set of nodes $\mathscr{N}$ connected with a set $\mathscr{E}$ of edges. One of the nodes are designated as the root, and the graph is connected in a topological sense. That is, given any pair of nodes in $\mathscr{N}$, a subset of $\mathscr{E}$ forms a path between them. We will refer to the root node as $\mathscr{N}_R$. We divide $\mathscr{N}$ into three subsets: The root node $\mathscr{N}_R$, interior nodes $\mathscr{N}_I$ and terminal nodes $\mathscr{N}_T$, see figure 3.1. The neighbours of node i and all edges meeting in node i will be denoted $\mathscr{N}_i$ and $\mathscr{E}_i$, respectively. Note that for $i \in \mathscr{N}_T$, $|\mathscr{N}_i| = |\mathscr{E}_i| = 1$. The edge $\mathscr{E}_i$, $i \in \mathscr{N}_R$ will be referred to as the root edge, while $\mathscr{E}_i$, $i \in \mathscr{N}_T$ will be referred to as terminal edges. If there are no circuits in the graph, we define it as a rooted tree $\mathscr{T}$.

Next, we give the graph a level structure. Let the node level L_m of the node i be the distance of the

shortest path between the root node and node i. We also assign a level to each edge so that the edge $e(i,j)$ has the same level as node j. All nodes except for the root node then have a belonging edge with the same level as itself. We let L_0 denote the root node level and L_M the maximum level in the tree, thus we have $m \in 0,1,2,...,M$ for the nodes and $m \in 1,2,3,...,M$ for the edges. The level structure is also demonstrated in Figure 3.1.

We want to distinguish between the visible vessel network and the sub-resolution, "invisible" network. We will do this by creating a subgraph $\mathcal{G}' \subseteq \mathcal{G}$ that contains nodes and edges in $\mathcal{T}$ up to a given level $L_{M'}$. The nodes at $L_{M'}$ are the terminal nodes of $\mathcal{G}'$ and will be denoted as $\mathcal{N}_{T'}$.

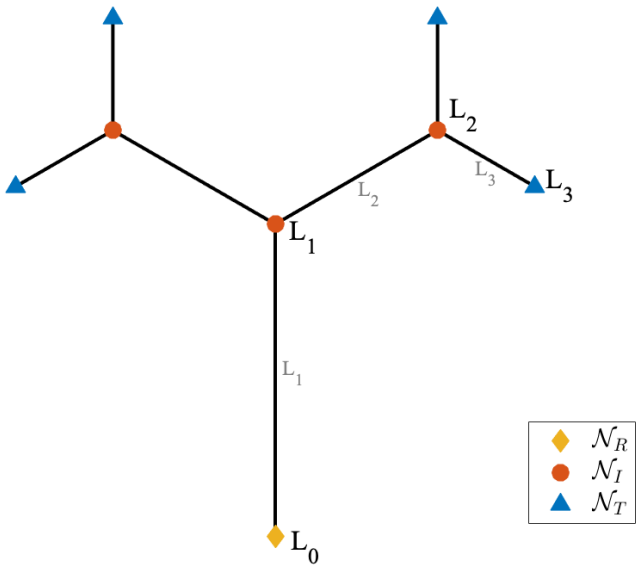

Figure 3.1: *A rooted tree with 1 root node (yellow diamond), 3 interior nodes (red circles) and 4 terminal nodes (blue triangles). The level structure is also illustrated. The node levels are written with black text and the edge levels in gray.*

3.2 Continuous formulation of the mathematical models

Here we present the governing equations building the two models. The constitutive laws for network flow (Hagen-Poiseuille) and domain flow (Darcy) are common for both models and are presented first, in Section 3.2.1 together with mass conservation equations and boundary conditions that also appears in both models. The models are distinguished in the coupling of the network and domain, leading to two different sets of equations which are handled in the next two subsections. In Section 4.3.1 we then consider the equations accounting for the reference model, and section 3.2.3 considers the coarse model.

3.2.1 Common governing equations

The domain pressure potential $p^D(\mathbf{x})$, $\mathbf{x} \in \Omega$ is chosen as primary variable. To each point $\mathbf{x} \in \Omega$ we assign a conductivity $K^D(\mathbf{x})$ given by Equation (2.13). Flow in the porous domain is then given by Darcy's law:

$$\text{(Flow in domain)} \qquad q^D = -K^D(\mathbf{x})\nabla p^D \tag{3.1}$$

In the network, we pressurize each node $i \in \mathscr{N}$ and denote the network pressure potential as p^N. To each edge we assign a length l, a radius r and a conductivity $K^N_{i,j}$ given by the Hagen-Poiseuille equation,

$$K^N = \frac{\pi r^4}{8\mu l}. \tag{3.2}$$

and the network flow from node i to j is then given by

$$\text{(Flow in network)} \qquad q^N_{i,j} = -K^N_{i,j}(p^N_j - p^N_i), i \in \mathscr{N}, j \in \mathscr{N}_i. \tag{3.3}$$

Common for both models is that mass must be conserved in the interior nodes of the graph. That is, for $i \in \mathscr{N}_I$, the sum of fluid flowing into the node must be equal to the sum of fluid flowing out, plus eventual external source/sink terms r^N_i:

$$\text{(Mass conservation in interior nodes)} \qquad -\sum_{j \in \mathscr{N}_i} q^N_{j,i} = r^N_i \quad i \in \mathscr{N}_I. \tag{3.4}$$

To close the system, Dirichlet boundary conditions have been set on the root node and on the boundary $\partial\Omega$. Throughout this thesis, we have used

$$p^N_i = 1 \quad i \in \mathscr{N}^R \qquad\qquad p^D = -1 \quad on \quad \partial\Omega \tag{3.5}$$

when solving the coupled system both with the reference and the coarse model.

3.2.2 Coupling of flow and pressure in the reference model

In the reference model, we let a graph $\mathscr{G}$ model the vessel network down to mesoscale level, and we couple the network to the Darcy domain directly through the terminal nodes $i \in \mathscr{N}_T$ of $\mathscr{G}$, see Figure 3.3. In order to couple the flow flux $q^N_{\mathscr{N}_i,i}$ to the flow in the domain, we now let each connection point between $\mathscr{N}_i$, $i \in \mathscr{N}_T$ and Ω be defined as its own domain, Ω_{T_i}. That is, the porous domain Ω has a "hole" at all places where the graph and the domain connects, in which each hole is a small, circular domain Ω_{T_i} with radius equal to the edge radius of $\mathscr{E}_i$, $i \in \mathscr{N}_T$, see figure 3.2. We then impose mass conservation in Ω and boundary conditions on $\partial\Omega_{T_i}$ to require that flow entering Ω is from the network only, entering through the boundary $\partial\Omega_{T_i}$. We end up with the following set of equations:

$$\text{(Mass conservation in domain)} \qquad \nabla \cdot q^D(\mathbf{x}) = r^D \quad \mathbf{x} \in \Omega \tag{3.6}$$

where r^D is any sources or sinks in the domain, and in this continuous formulation considered to be zero.

(Neumann boundary conditions at terminal nodes) $$\int_{\partial\Omega_{T_i}} q^D(\mathbf{x}) \cdot v_n \, dl = q^N_{\mathcal{N}_i,i} \qquad \mathbf{x} \in \partial\Omega_{T_i}, \quad \forall i \in \mathcal{N}_T \tag{3.7}$$

Where v_n is the outward normal vector on $\partial\Omega_{T_i}$.

(Dirichlet boundary conditions at terminal nodes) $$p^D(\mathbf{x}) = p^N_i, \qquad \mathbf{x} \in \partial\Omega_{T_i}, \quad \forall i \in \mathcal{N}_T \tag{3.8}$$

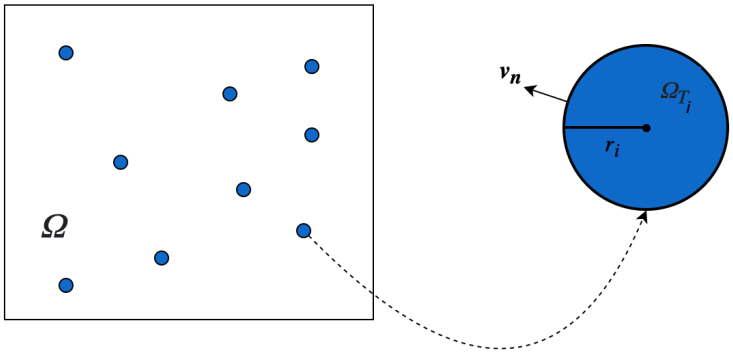

Figure 3.2: *Each intersection point between terminal node $\mathcal{N}_i$, $i \in \mathcal{N}_T$ and Ω forms a domain Ω_{T_i} withing Ω. v_n is the normal vector pointing outwards from $\partial\Omega_{T_i}$.*

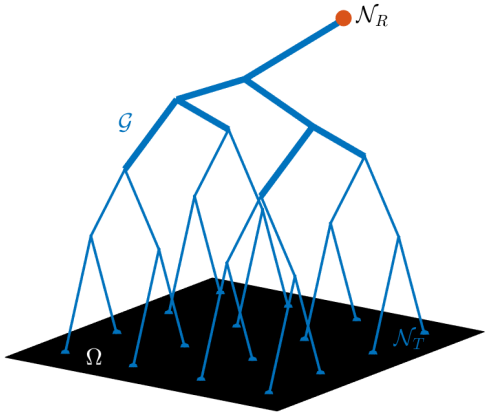

Figure 3.3: *Illustrative figure of the reference model. $\mathcal{G}$ is the graph both modelling the macroscale network and mesoscale network. The network is coupled to the domain Ω through the micro terminal nodes $\mathcal{N}_T$, illustrated with blue dots.*

3.2.3 Coupling of flow and pressure in the coarse model

The coarse model is an up-scaled approximation of the reference model, where we replace the network that is taken to be unknown with a continuous, linear flow model. That is, we cut $\mathcal{G}$ from $L_{M'}$ to L_M, and keep only the subgraph $\mathcal{G}'$ modelling the macroscale network, see Figure 3.4. Now, the flow transferring from terminal node $i \in \mathcal{N}_{T'}$ to $\mathbf{x} \in \Omega$ is described as

$$\text{(Flow transferring from network to domain)} \qquad q_i^T(\mathbf{x}) = -K_i^T(\mathbf{x})(p^D(\mathbf{x}) - p_i^N), \quad i \in \mathcal{N}_{T'} \tag{3.9}$$

involving the spatially distribution transfer parameter $K_i^T(\mathbf{x})$. $K_i^T(\mathbf{x})$ can be considered as a conductivity for the total "path" from terminal node to domain, analogous to K^N for one graph edge. The calculation of K^T will be demonstrated in the next chapter. Now we consider the coupling of the flow from network to domain. To ensure conservation of mass in the domain Ω, we require that the sinks in Ω is equal to the terminal node sources, that is,

$$\text{(Mass conservation in domain)} \qquad \nabla \cdot \mathbf{q}^D - \sum_{i \in \mathcal{N}_T} q_i^T(\mathbf{x}) = 0 \qquad i \in \mathcal{N}_T, \quad \mathbf{x} \in \Omega. \tag{3.10}$$

Then to ensure conservation of mass in the terminal nodes, we require that fluid flowing from terminal node i to point $\mathbf{x}$ in the Darcy domain is equal to the fluid flowing through the terminal edge ending in i,

$$\text{(Mass conservation in terminal nodes)} \qquad \int_\Omega q_i^T(\mathbf{x}) d\mathbf{x} - q^N_{\mathcal{N}_i,i} = 0, \qquad i \in \mathcal{N}_T, \quad \mathbf{x} \in \Omega. \tag{3.11}$$

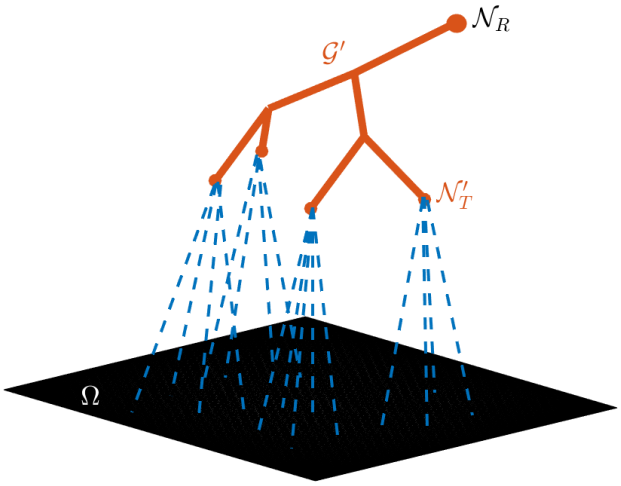

Figure 3.4: *Illustrative figure of the coarse model. $\mathcal{G}'$ is the macroscale network, a subgraph of $\mathcal{G}$ where $\mathcal{N}_{T'}$ is the set of its macro terminal nodes. The mesoscale network is "cut away", and Equation (3.9) describes the flow that is distributed from $i \in \mathcal{N}_T$ to $\mathbf{x} \in \Omega$.*

4 Methods

This chapter concerns the methods used in the numerical implementation of the model, as well as methods for verification of the code. It contains the following sections:

Section 4.1 covers the generation of the three different graphs modelling the mesoscale network in the reference model, in addition to the numerical solving of the network flow.

In Section 4.2 we describe the numerical method used to solve the flow equations in the Darcy domain, which is a Finite Volume Two Point Flux Approximation (FV-TPFA) method.

Section 4.3 presents the discretized coupling of the network and Darcy flow. Section 4.3.1 concerns the reference model, where the flow and pressure is coupled using the *Peaceman correction*, a method stemming from the numerical solving of flow in reservoirs and wells. In 4.3.2 we present how K^T is numerically calculated and include it in the linear system for the coarse model.

Finally, Section 4.4 concerns the verification methods of the code. We verify the FV-TPFA method and the coupling in the reference model using well known test cases. Also, we derive methods for verifying the calculation of K^T and the coarse model.

4.1 Network generation and flow

4.1.1 Deterministic tree

The first network we consider herein is a binary, symmetric fractal tree. This will be referred to as the *deterministic tree* because its structure is given by its "initial configuration" values. The symmetry as well as the deterministic feature makes this tree suitable for observing effects of varying isolated variables when experimenting. Since the tree is symmetric, all terminal nodes and edges will be at the same level L_M. The length and radii of the edges with level L_m, $m = 1,2,...,M$ is given in a fractal sense by assigning a constant reduction factor $0 < \alpha_r \leq 1$ to the edge radii such that $\alpha_r := \frac{r_m}{r_{m+1}}$ and, similarly, $0 < \alpha_l \leq 1$ to the edge length such that $\alpha_l := \frac{l_m}{l_{m+1}}$. Thus, all edge lengths and radii may be found from the length and radius of the root edge and the respective reduction factor. The last value we assign to the tree is a constant bifurcation angle θ. With certain choices of θ and α_l, we get a space filling tree as in Figure 4.1.

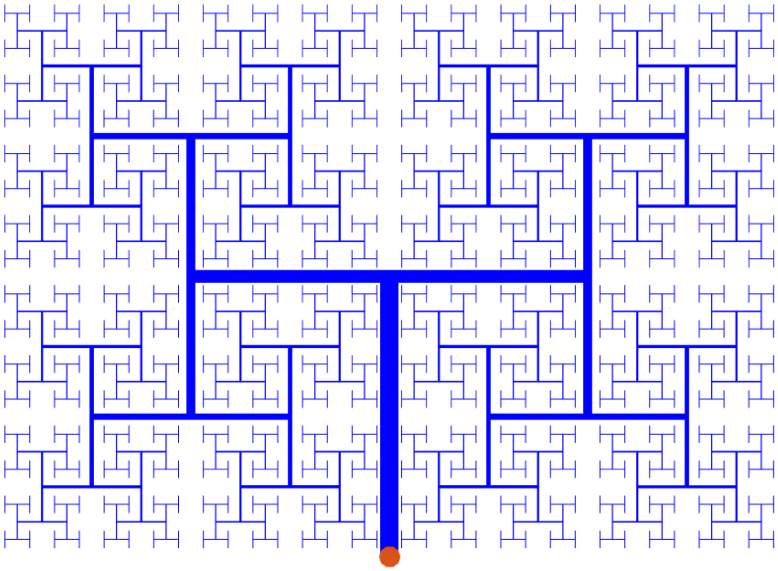

Figure 4.1: *A space-filling deterministic tree in the domain* $\Omega := x \in [0,1], y \in [0,1/\sqrt{2}]$ *with maximum level* $M = 11$, $l_1 = 1/2\sqrt{2}$, *length reduction factor* $\alpha_l = \frac{1}{\sqrt{2}}$, *radius reduction factor* $\alpha_r = 0.7$ *and bifurcation angle* $\theta = 90°$. *The red dot marks the root node.*

The tree was generated using a recursive algorithm with the initial configurations as input, where the code proceeds the following steps:

1. Place the root node $\mathcal{N}_R$ at the midpoint of the horizontal axis and set the maximum level M.
2. Construct main stem rooted in $\mathcal{N}_R$ with given length l_1, radius r_1 and a 90° angle with the horizontal.
3. From the end node of the current edge e_i, construct two new edges with bifurcation angle $\pm\theta$ with the line of direction to the current edge with length $l_i\alpha_l$ and radius $r_i\alpha_r$.
4. Repeat step 3 while the node level of the end-node is less than M.

4.1.2 Diffusion limited aggregation generated network

The Diffusion Limited Aggregation (DLA) model is an idealized model for the growth process of cluster formations such as dendrites, dust and bacteria, where the growth is limited by the diffusion of matter to the cluster, developed by Witten and Sander (1981). It has also been suggested that this growth mechanism is the driving force in vascular growth from pre-existing vascular network (angiogenesis)

(Fleury & Schwartz, 1999). The process behind the algorithm is simply described by J. D. Murray (2002): "Diffusion limited aggregation is a diffusion process whereby particles exhibit a random walk and when a particle comes into contact with another particle it sticks to it and can no longer move". The code used herein was found at GitHub (https://github.com/natter1/playground/blob/master/my_dla_optimization.py) and builds the network through the following steps:

- A seed particle is placed at the center of the domain
- A new particle (random walker) is released at the boundary of the domain
- The particle does a random walk until it comes in touch with another particle and sticks to it
- The process is repeated n (number of particle) times

The network complexity is hence determined by setting the number of particles involved in the generation. The output file was converted from a binary structure to a graph structure in MATLAB using the function *npy2tree.m*, see GitHub repository.

As opposed to the deterministic tree, the structure of the DLA network is a result from a random process, and the only factor to be determined is the number of particles involved in the generation. Figure 4.2 is an example of how a network generated with 16000 particles may look like. The root node is here placed manually at a central network node where all the "main branches" meet.

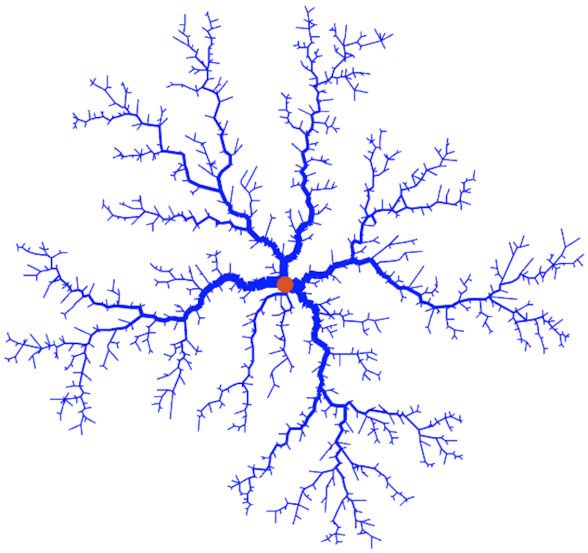

Figure 4.2: *A graph generated by diffusion limited aggregation with 16000 particles in a square domain. The red dot marks the root node.*

Radius setup for unstructured trees

Previously, we assigned each edge a radius by setting the root edge radius and a reduction factor, thus obtaining progressively smaller radii with increasing level. Since the deterministic network is symmetric, we obtain the same radius at all terminal edges. This network is however unstructured, and we have terminal nodes at all levels, both directly linked to the main stems as well as in the outer most branches. Setting the radii the same way will result in some unrealistic short and wide terminal edges at low levels. Instead, we let all terminal edges have the same radius r_T. Then we define one of the root edges as the main stem of the network and set its radius to $r_R > r_T$. To assign the correct radius to all edges, we now consider an inverse level system in which all $i \in \mathcal{N}_T$ has level L_0^{inv} and the rest of the nodes has node level L_n^{inv}, $n = 1,2,...,M$ according to their distance from the the terminal node. For nodes that lies on several root node-terminal node paths, we choose the highest n, and the root node thus get a node level L_M^T, see Figure 4.3 for illustration.

We now derive the radius reduction factor α_r from r_R and r_T in order to assign the correct radius to each edge. We start by considering the longest root node-terminal node path in the network. The radius at L_1 is set to r_R, thus the radius at L_2 must be given by

$$r_2 = r_R \alpha_r, \tag{4.1}$$

and at L_3 by

$$r_3 = r_R \alpha_r^2, \tag{4.2}$$

and so on. Since there are M levels in the tree, the terminal edge is given by

$$r_T = r_R \alpha_r^{M-1}. \tag{4.3}$$

We solve for α_r by taking the logarithm on each side:

$$(M-1) ln(\alpha_r) = ln\left(\frac{r_T}{r_R}\right), \tag{4.4}$$

and we can express the reduction factor as follows:

$$\alpha_r = e^{\beta}, \tag{4.5}$$

where

$$\beta = ln\left(\frac{r_T}{r_R}\right)\frac{1}{M-1}. \tag{4.6}$$

We now set α_r according to this setup. The edge $e_{i,j}$ is assigned a radius according to the node level n of j, that is

$$r_n = \frac{r_T}{\alpha_r^n} \qquad n = 0,1,2,...M-1 \tag{4.7}$$

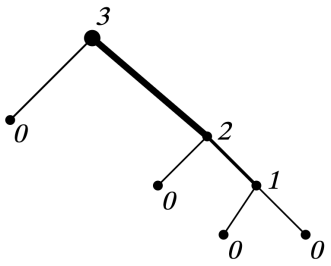

Figure 4.3: *Illustration of the inverse level system and the resulting radius setup. The root node is marked with a bigger dot, and has level L_3^{inv} since the longest root node-terminal node path in the graph has length 3. All terminal nodes has level L_0^{inv}. Notice that the node at L_2^{inv} has been given its node level according to the longest root node-terminal node path that it is part of, and not according to the nearest terminal node.*

4.1.3 Rapidly exploring random tree

The Rapidly-exploring random tree (RRT) was invented by Kuffner and LaValle (2011) as a tool for path planning, and is used as test case herein because of its space filling and fractal (Burch & Weiskopf, 2013) properties. The aim of the algorithm is to search for and cover unexplored areas of a given domain Ω by building the RRT.

Given a start position x_{init} and the resulting amount of terminal nodes K, the pseudocode used for the generation reads:

$GENERATE.RRT(x_{init}, K, \Omega)$
while $|\mathscr{N}_T| < K$ **do**
  $x_{rand} \leftarrow RandomState(\Omega)$
  $x_{near} \leftarrow NearestNeighbor(x_{rand}, \mathscr{T})$
  $\mathscr{T}.AddNode(x_{new})$
  $\mathscr{T}.AddEdge(x_{near}, x_{new})$
end while
return $\mathscr{T}$

In $RandomState(\Omega)$, a random position x_{rand} in the domain is found. x_{near} is then the nearest neighbour in the tree to x_{rand}. x_{near} may also be an edge that is closer to x_{rand} than the closest node. In that case, a new edge is made as a normal to this edge. If x_{near} is a node, then the new edge is made as a normal from x_{rand} to the closest edge connected to that node. An exception is made if the angle between the vector from x_{rand} to x_{near} and the closest edge is more that 90°. The new edge is then constructed between the nodes x_{rand} and x_{near}. This results in a tree where most angles are 90°, see Figure 4.4. For the radii we use the same setup as with the DLA generated network.

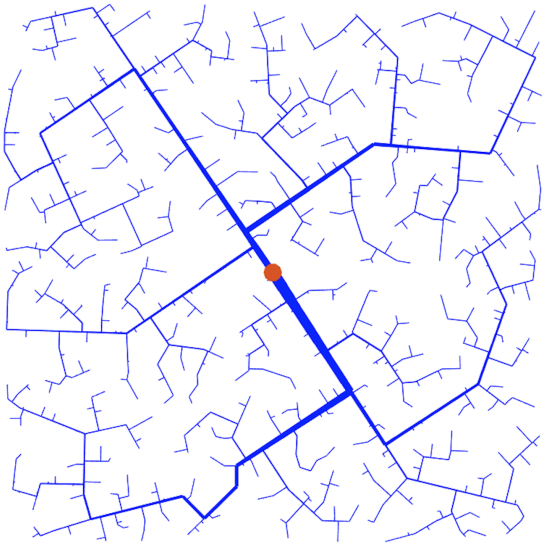

Figure 4.4: A rapidly exploring random tree with 500 terminal nodes in a square domain.

4.1.4 Discrete network flow

Flow in the discrete network is calculated according to the Hagen-Poiseuille law. We will use Dirichlet boundary conditions

$$\mathbf{p}_i = 1, \quad i \in \mathcal{N}_R \qquad\qquad \mathbf{p}_i = -1, \quad i \in \mathcal{N}_T \tag{4.8}$$

when solving for flow in the network only. Conservation of mass in the interior nodes is assured through Equation (3.4), and solved together with Equation (3.3) we get the following system of equations:

$$\begin{bmatrix} \frac{1}{K^N} & \nabla^{\mathbf{h}} \\ \nabla^{\cdot\mathbf{h}} & 0 \end{bmatrix} \begin{bmatrix} \mathbf{q}^N \\ \mathbf{p}_I^N \end{bmatrix} = \begin{bmatrix} \mathbf{p}_D^N \\ 0 \end{bmatrix}$$

where $\nabla^{\mathbf{h}}$ and $\nabla^{\cdot\mathbf{h}}$ are connectivity matrices working as discrete gradient and discrete divergence operators, respectively, and $\mathbf{p}_D^N$ is a $|\mathcal{N}| \times 1$ column vector with Dirichlet boundary condition values on the Dirichlet node entries.

4.2 Finite volume method (FVM) on Voronoi grid

The flow equations for the Darcy domain have been discretized using a cell centered finite volume scheme. The finite volume method (FVM) involves dividing the domain into smaller subdomains, or control volumes, and then evaluating the PDE of interest by integrating over the control volumes. Here, the control volumes are the cells resulting from the Voronoi diagram generated from the terminal nodes of the invisible vessel tree, see Figure 4.5. Each cell can therefore be though of as a distribution area for the blood from its belonging terminal node. However, we will for now consider the porous domain as

an isolated system at steady state without any flow contributions from the network, while the coupling will be considered in the next section. Thus, for a Voronoi grid cell ω_i we have the following mass conservation equation

$$\int_{\omega_i} \nabla \cdot \mathbf{q}^D dV = \int_{\omega_i} r^D dV \tag{4.9}$$

where r^D is any sources or sinks other than blood from feeding vessels. The next step is to convert the volume integrals into surface integrals using the divergence theorem, which states that

$$\int_{\omega_i} \nabla \cdot \mathbf{q}^D dV = \int_{\partial\omega_i} \mathbf{q}^D \cdot v_n dA \tag{4.10}$$

and then employ a flux approximation method to evaluate the fluxes over the boundaries of the control volume.

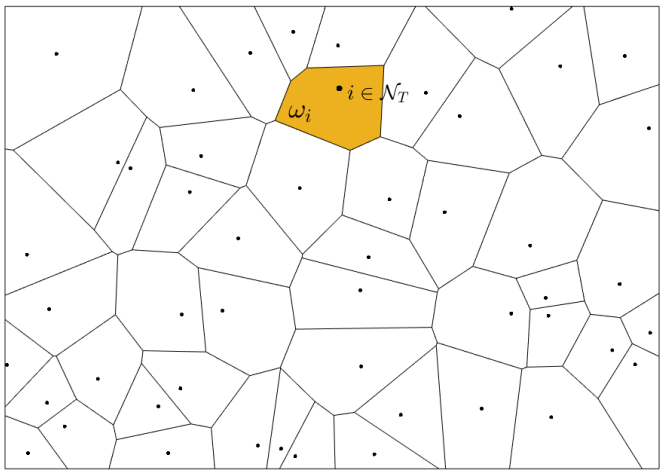

Figure 4.5: *A Voronoi diagram generated from the terminal nodes $i \in \mathcal{N}_T$ of the graph, shown as dots within each cell ω_i.*

This has been done using a two-point flux approximation (TPFA) scheme, where the normal component flux over a boundary segment σ_{ij} is approximated using the pressure potential values in the two volumes ω_i, ω_j on each side of the segment. That is, each Voronoi cell ω_i is assigned a discrete pressure value $\mathbf{p}_i$ in its center, and each boundary segment a flux to its midpoint. This discrete flux $\mathbf{q}^D_{i,j}$ over the boundary segment σ_{ij} between two adjacent cells ω_i and ω_j is approximated according to Darcy's law, Equation (2.9):

$$\mathbf{q}^D_{i,j} \cdot v_n = K^D \frac{(\mathbf{p}_i - \mathbf{p}_j)}{\Delta x_{ij}} \tag{4.11}$$

where Δx_{ij} is the distance between the centers of ω_i and ω_j. Now we can write the discrete formulation of Equation (4.9) in terms of Equation (4.11) inserted into the surface integral in Equation (4.10). We take the value of r^D to be constant within the cell, so the right hand side integral is just this value multiplied

with the cell area. By iterating over the neighbouring cells j of the cell i, the discrete formulation of Equation (4.9)-(4.10) thus reads

$$\sum_j \mathbf{q}_{i,j}^D \cdot v_n = \mathbf{r}_i^D A_i \tag{4.12}$$

where l_{ij} is the length of σ_{ij}.

The fluxes over the boundary segments that is also a part of the boundary $\partial\Omega$ is approximated by constructing a "ghost cell" $\tilde{\omega}_i$ on the adjacent side of the segment. With a Dirichlet boundary condition $\mathbf{p}_{BC}$ on $\partial\Omega$, we let the pressure value $\tilde{\mathbf{p}}_i$ in the ghost cell be given by

$$\mathbf{p}_{BC} = \frac{\mathbf{p}_i + \tilde{\mathbf{p}}_i}{2}. \tag{4.13}$$

If we let the length of a segment that is both a boundary of a cell ω_i and also a part of $\partial\Omega$ be denoted $\tilde{l}_i$ and the distance between the center of ω_i and $\tilde{\omega}_i$ be denoted $\tilde{\Delta x_i}$, then the flux over this segment is given by

$$\tilde{\mathbf{q}}_i = 2K^D \frac{(\mathbf{p}_i - \mathbf{p}_{BC})\tilde{l}_i}{\tilde{\Delta x_i}} \tag{4.14}$$

Let Nc be the number of cells, and Ns be the number of cell segments. To integrate over the whole domain, a $Nc \times Ns$ cell-to-segment connectivity matrix has been constructed by iterating over all segments in all cells and setting the matrix values as follows:

$$C_{i,j} = \begin{cases} 1 & \text{if segment j is a boundary segment of } \omega_i \\ -1 & \text{if segment j is a boundary segment of } \omega_i\text{, but already accounted for at a neighbouring cell} \\ 0 & \text{otherwise.} \end{cases}$$

This matrix will work as a discrete divergence, and its transpose as a discrete gradient. For the sake of clarity we rename the matrix and let $C = \nabla\cdot^{\mathbf{TPFA}}$ and $C^T = \nabla^{\mathbf{TPFA}}$. $l_{i,j}$ and $\Delta x_{i,j}$ for each segment is collected in the vector B. For simplicity we do not consider the effect of any source terms, thus r^D = 0. On the right hand side we then only have the Dirichlet terms. Let B_{BC} be a $Ns \times Ns$ diagonal matrix with $\frac{2\tilde{l}_i}{\Delta\tilde{x}_i}$ on the Dirichlet row entries according to Equation (4.14), and let $\mathbf{P}_{BC}^D$ be a $Nc \times 1$ vector with Dirichlet boundary values $\mathbf{p}_{BC}$ on the Dirichlet entries. According to Equation (4.12) we obtain the following:

$$\nabla\cdot^{TPFA} K^D \nabla^{TPFA} B\, \mathbf{p}^D = \nabla\cdot^{TPFA} K^D B_{BC} \mathbf{P}_{BC}^D \tag{4.15}$$

The code for the generation of the Voronoi diagram is from Sievers (2022), and the coordinates for the terminal nodes where used as input argument. The cell area were found using the MatLab built-in function *polyarea*.

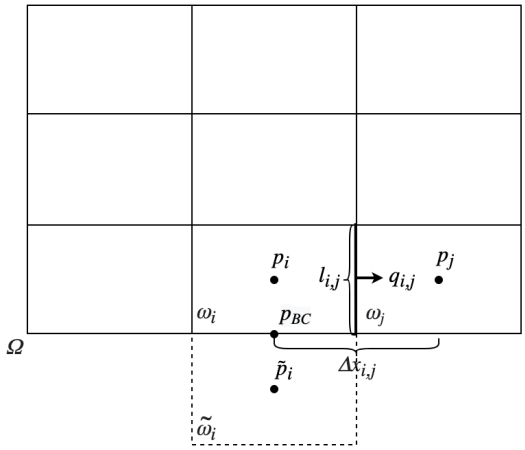

Figure 4.6: *Illustration of the TPFA method. To each cell center we assign a pressure value, and across each segment $\sigma_{i,j}$ between ω_i and ω_j we assign a flux $q_{i,j}$. This flux is calculated according to Equation (4.11), using the pressure values on each side of $\sigma_{i,j}$, the length $l_{i,j}$ and the distance $\Delta x_{i,j}$ between the cell center of ω_i and ω_j. The fluxes across segments that are part of $\partial\Omega$ are calculated according to Equation (4.14), and involves the construction of a ghost cell $\tilde{\omega}_i$.*

4.3 Coupling between network and porous domain

Next, we consider the discrete coupling of the network and the Darcy domain. For each model, this is done by solving for $\mathbf{p}^D$, $\mathbf{q}^N$ and $\mathbf{p}^N$ simultaneously in a system of equations. Let

$$\Delta^{TPFA} := Div\ K^D\ Grad\ B, \qquad \mathbf{f}^{TPFA} := \nabla.^{TPFA} K^D B_{BC} \mathbf{P}^D_{BC}$$

and let Ne, Nn, Ntn and Nc be the number of edges, nodes, macro terminal nodes and cells, respectively. Note that Nc is the same as the number of micro terminal nodes, thus, we will use Nc for both. For each model we now construct a block matrix where each row corresponds to a flow equation, either a constitutive equation, a mass conservation equation, or both solved together.

4.3.1 Reference model

The network equations is the same as in Section 4.1.4, but on the right hand side we have now only the Dirichlet root pressure, as the outlet-pressure is set on $\partial\Omega$, according to Section 3.2.1. We hence denote the right hand side of the network equations as $\mathbf{p}^N_R$, which is a $|\mathscr{N}| \times 1$ column vector with root node pressure on the root node entry. Next, we solve the flow in the Darcy domain, which must be coupled to the network flow to ensure mass conservation. Now, discretizing Equation (3.6)-(3.8) requires a grid with mesh size $h << r_i$, where r_i is the radius of Ω_{T_i}, in order to calculate the flow distribution around a terminal node, which would lead to an expensive method for very small vessel radii. Therefore, for the numerical implementation of the reference model, we consider instead each terminal node as a source

point in each Voronoi grid cell, and let

$$\mathbf{r}^D A_{\omega_i} = \mathbf{q}^N_{\mathcal{N}_i,i} \qquad i \in \mathcal{N}_T \tag{4.16}$$

We ensure mass conservation in the domain by inserting Equation (4.16) into Equation (4.12) to obtain

$$\sum_j \mathbf{q}^D_{i,j} \cdot v_n = \mathbf{q}^N_{\mathcal{N}_i,i} \tag{4.17}$$

for each cell ω_i, $i \in \mathcal{N}_T$ and for all of its neighbours ω_j. This make up line 3 in the system matrix below, where the matrix I_{TE} is a $Nc \times Ne$ connectivity matrix between cells and terminal edges.

At last, we must couple the network and the domain pressure, and for this we use the results from Peaceman (1978). The work of Peaceman considers the numerical solving of the pressure near the well in a reservoir using the TPFA method on a uniform, squared grid. We use the source vessel and the distribution area (surrounding tissue) as analogy to the well and the surrounding reservoir. What Peaceman found was that for a pressure distribution around a well given by

$$\mathbf{p}^D(r) = \mathbf{p}^N_i - \frac{\mathbf{q}^N_{\mathcal{N}_i,i}}{2\pi K^D} \ln\left(\frac{r}{r_i}\right), \qquad i \in \mathcal{N}_T, \tag{4.18}$$

the pressure $\mathbf{p}^D_i$ in a cell ω_i (well block) is equal to the flowing pressure at $r = 0.2\Delta x$, where Δx is the width of the grid cell in a uniform, squared grid. Here we use $\Delta x = \sqrt{A_\omega}$, and for the pressure $\mathbf{p}^D_i$ in the cell ω_i surrounding the terminal node $i \in \mathcal{N}_T$ we then have

$$\mathbf{p}^D_i = \mathbf{p}^N_i - \frac{\mathbf{q}^N_{\mathcal{N}_i,i}}{2\pi K^D} \ln\left(\frac{0.2\Delta x_i}{r_i}\right), \qquad i \in \mathcal{N}_T. \tag{4.19}$$

The adjustment of the cell pressure according to the findings of Peaceman (1978) is called the *Peaceman correction*, and we have illustrated how the pressure in each cell is corrected for in Figure 4.7. To solve this numerically, matrix PC of size $Nc \times Ne$ is constructed and added to the system of equations. This matrix has the last term in Equation (4.19) on the respective grid cell-terminal edge entries and zero elsewhere. We finally obtain the following block matrix:

$$\begin{bmatrix} 0 & \frac{1}{K^N} & \nabla^{\mathbf{h}} \\ 0 & \nabla^{\cdot\mathbf{h}} & 0 \\ \Delta^{TPFA} & I_{TE} & 0 \\ I & PC & -I_{TN} \end{bmatrix} \begin{bmatrix} \mathbf{p}^D \\ \mathbf{q}^N \\ \mathbf{p}^N \end{bmatrix} = \begin{bmatrix} \mathbf{p}^N_R \\ 0 \\ \mathbf{f}^{TPFA} \\ 0 \end{bmatrix}$$

The system of equations is then solved using the MATLAB backslash operator.

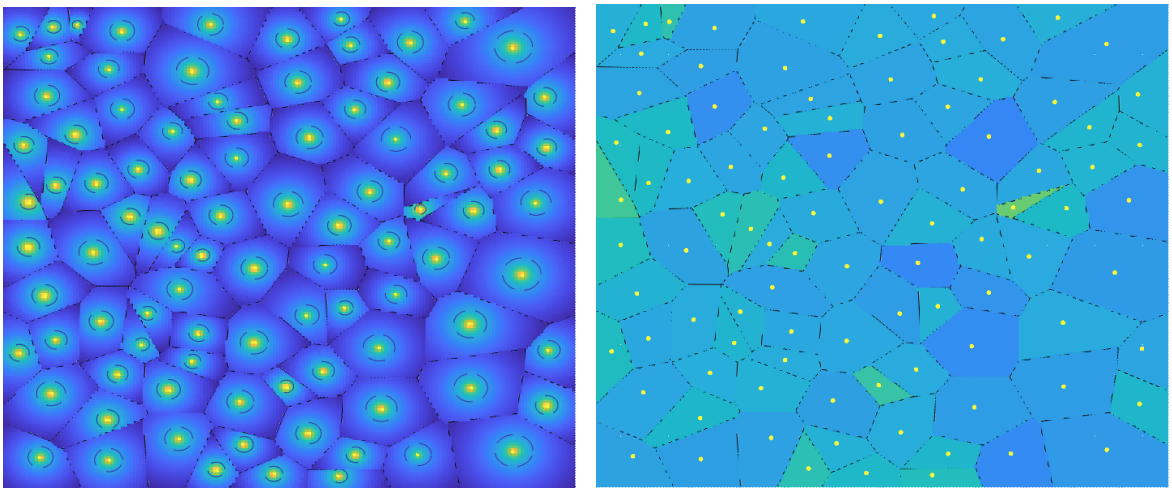

(a) *Peaceman correction in each cell.* (b) *Average pressure in cells.*

Figure 4.7: *Illustration of how the Peaceman correction is used. In (a), the pressure distribution from each node according to Equation (4.18) is plotted in its respective Voronoi grid cell. Light colors correspond to high pressure values. The yellow dots thus correspond to the fluid pressure in the source vessel (terminal node pressure), and the pressure decreases rapidly as we move away from the vessel. The dashed circle in each cell correspond to $r = 0.2\Delta x$ and we set the pressure at this point as the average grid cell pressure in the TPFA method. This pressure value corresponds to that plotted in the same cells in (b).*

4.3.2 Coarse model

The first step is to obtain an expression for the transfer parameter K^T. From Equation (3.9) we obtain

$$K_i^T(\mathbf{x}) = -\frac{q_i^T(\mathbf{x})}{p^D(\mathbf{x}) - p_i^N}. \tag{4.20}$$

We now let $K_i^T(\mathbf{x})$ be a set of piece-wise constants within each cell, that is,

$$K_i^T(\mathbf{x}) = K_i \qquad \forall\, \mathbf{x} \in \omega_j, \quad \forall\, j \in \mathcal{N}_T, \quad \forall\, i \in \mathcal{N}_{T'} \tag{4.21}$$

Since we by that assume $q_i^T(\mathbf{x})$ to be constant within ω_j, we have, from Equation (3.11), that

$$q_i^T(\mathbf{x}) = \frac{\mathbf{q}^N_{\mathcal{N}_j,j}}{A_{\omega_j}} \tag{4.22}$$

Let the pressure in the macro terminal nodes be denoted $\mathbf{p}_i^N$ and the micro terminal node pressure is denoted $\mathbf{p}_j^N$. The network transfer parameter is then given by

$$K_i = \frac{\mathbf{q}^N_{\mathcal{N}_j,j}}{A_{\omega_j}(\mathbf{p}_i^N - \mathbf{p}_j^N)}, \qquad i \in \mathcal{N}_{T'}, \quad j \in \mathcal{N}_T \tag{4.23}$$

When solving for K^T, we use the network only with Dirichlet boundary condition on all open ends according to Section 4.1.4. With an expression for K^T, we can now solve the linear system for the coarse model. We have an extra component in the system, namely the transfer flux $q_i^T(\mathbf{x})$. When coupling the network and domain, we now have

$$\sum_j \mathbf{q}_{i,j}^D \cdot v_n = \mathbf{q}_i^T(\mathbf{x}) \cdot A_{\omega_i} \tag{4.24}$$

Row 2-3 is the same network equations as before, and in row 4-5 we solve Equation (4.22) and Equation (4.21), respectively. The matrix K^T is a $Nc \times Ntn$ matrix where $K_{j,i}^T$ is the K^T value for the j^{th} micro terminal node and the i^{th} macro terminal node. Thus, the matrix K^T is a somehow weighted connectivity matrix between macro and micro terminal nodes. We end up with the following system matrix. Here, the network pressure is split into two vectors, one for the interior nodes $\mathbf{p}_I^N$ and one for the terminal nodes $\mathbf{p}_T^N$, for the sake of clarity.

$$\begin{bmatrix} \Delta^{TPFA} & 0 & 0 & 0 & A_{\omega_i} \\ 0 & \frac{1}{K^N} & \nabla^{\mathbf{h}} & \nabla^{\mathbf{h}} & 0 \\ 0 & \nabla \cdot^{\mathbf{h}} & 0 & 0 & 0 \\ 0 & I_{TE} & 0 & 0 & A_{\omega_i} \\ K^T & 0 & 0 & -K^T & I \end{bmatrix} \begin{bmatrix} \mathbf{p}^D \\ \mathbf{q}^N \\ \mathbf{p}_I^N \\ \mathbf{p}_T^N \\ \mathbf{q}^T \end{bmatrix} = \begin{bmatrix} \mathbf{f}^{TPFA} \\ \mathbf{p}_R^N \\ 0 \\ 0 \\ 0 \end{bmatrix}$$

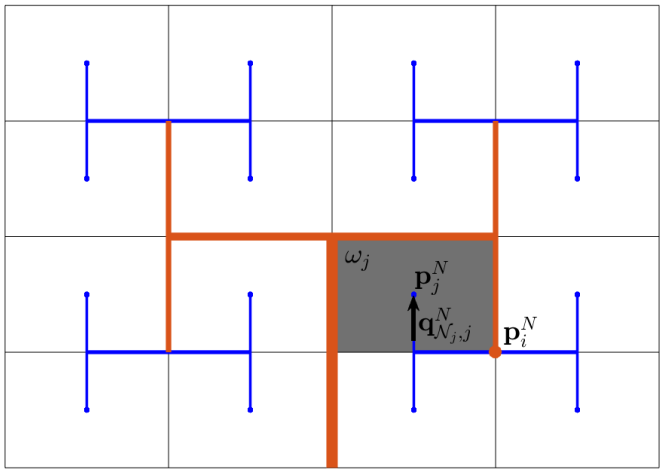

Figure 4.8: *This figure shows the variables included in Equation (4.23). p_i^N is the pressure in the macro terminal node, and p_j^N the pressure in the micro terminal node, $q_{\mathcal{N}_i,i}^N$ is the flux in the terminal edge and A_{ω_i} is the area of the cell ω_i.*

4.4 Methods for code verification

4.4.1 Verification of the Two Point Flux Approximation (TPFA) method

The TPFA method has been verified by solving the test problem

$$-\nabla \cdot \nabla u = f(x,y), \quad x,y \in [0,1] \tag{4.25}$$

$$u = 0, \qquad \text{on} \quad \partial\Omega \tag{4.26}$$

which has the analytical solution

$$u = (1-x)(1-y)xy$$

and the corresponding flux function

$$f(x,y) = 2y - 2y^2 + 2x - 2x^2$$

This is a commonly used test problem, and it is known that the order of convergence is 2 when solving this problem on a squared lattice. This has been proven to hold, see Appendix A. In this work, however, the grid is a Voronoi diagram based on the terminal nodes of a randomly generated tree. The grid is therefore irregular, with cells of different sizes and shapes. Normal grid refinement can not be performed, instead, a new tree with more terminal nodes is generated to obtain a finer grid. An expected convergence rate can therefore not be predicted analytically, but the order of convergence may be found numerically by running several tests and look at the average error.

Here, one convergence test involves "refining" the grid 5 times by doubling the number of terminal nodes and thereby also the number of grid cells. u_i^h is, according to the method, approximated on each cell ω_i, and the analytical value is calculated at the cell center (x_i, y_i). The error is measured in the L^2-norm, that is,

$$e = \sqrt{\sum_i u(x_i,y_i) - u_i^h)^2 A_{\omega_i}} \tag{4.27}$$

Due to varying results as a consequence of the randomly generated and irregular grid, several test has been performed and the average error is considered. See Section 5.1.1 for results.

4.4.2 Verification of the coupled system

To verify the system as a whole, that is, the network coupled with the Darcy domain, we use as a test problem the Laplace equation with a Dirac type source term:

$$-\nabla \cdot K^D \nabla p = q^0 \delta(r) \quad in \quad \Omega \tag{4.28}$$

where

$$\delta(r) = \begin{cases} 1/\pi r_0^2 & \text{if } 0 \leq r \leq r_0 \\ 0 & \text{if } r > r_0 \end{cases} \tag{4.29}$$

where r_0 is the radius of the source edge providing the flux q^0. The solution is the fundamental solution to the Laplace equation in 2D:

$$p = -\frac{q^0}{2\pi K^D} \ln(\frac{r}{r_0}) \qquad r > r_0$$

When solved numerically, we used a grid with size $h >> r_0$.

Setup

Consider $\Omega := \{x \in [-1,1], y \in [-1,1]\}$ coupled with a network where we have a Neumann boundary condition q^0 on the edge $\mathscr{E}_i$, $i \in \mathscr{N}_R$, $|\mathscr{E}_i| = 1$, and with an arbitrary number of terminal nodes. We let one terminal node be the source node of the domain, and place it in the middle, i.e., the origin. The conductivity in all terminal edges are set to zero except for the one leading to the source node, which we refer to as the source edge. On $\partial\Omega$, we set Dirichlet boundary conditions $p_{BC} = -\frac{q^N}{2\pi K^D} ln(\frac{r_{BC}}{r_0})$ on the midpoint of the boundary segment of the cell. r_{BC} denotes the distance from the source node to the boundary, and r_0 denotes the radius of the source edge. Now, we solve for the pressure $\mathbf{p}^D$. The error was measured in the L^2-norm, see Equation (4.27).

4.4.3 Verifying the calculations of the transfer conductivity

With the deterministic tree, we can derive the expression for the transfer function using only its initial configuration. This will here be used as a way of verifying the code by comparing the before hand calculated value of K^T with that calculated by the code. Since the tree is binary and completely symmetric both with respect to length and radius of the edges, the resistance in a path between a macro and micro terminal node is the same everywhere. In other words, the transfer function is expected to be constant for the whole tree.

To derive the analytical K^T from Equation (4.23), we need expressions for the pressure value at the macro terminal node (which will here be an arbitrarily chosen interior node), an expression for the flux in the terminal edges and the for cell areas.

Now let p_m and q_m be the pressure and flux at level L_m, respectively. The edge between the two nodes p_{m-1} and p_m will experience a pressure drop given by the Hagen-Poiseuille equation,

$$p_{m-1} - p_m = (K_m^N)^{-1} q_m \qquad m = 1, 2, ..., M. \tag{4.30}$$

Since the tree is binary and symmetric, the flux will be divided equally at each bifurcation point, and may be expressed in terms of q_1 as

$$q_m = \frac{q_1}{2^{m-1}} \qquad m = 1,2,...,M \tag{4.31}$$

The edge conductivity K_m^N will be equal for edges at the same level, and since the length and radius at level L_m may be expressed in terms of the root edge as

$$L_m = \alpha_l l_{m-1} = \alpha_l^{m-1} l_1 \quad \text{and} \quad r_m = \alpha_r r_{m-1} = \alpha_r^{m-1} r_1 \qquad m = 1,2,...,M \tag{4.32}$$

For the conductivity we have

$$K_1^N = \frac{\pi r_1^4}{8\mu l_1}, \quad K_2^N = \frac{\pi r_1 \alpha_r)^4}{8\mu l_1 \alpha_l}, \quad K_3^N = \frac{\pi (r_1 {\alpha_r}^2)^4}{8\mu l_1 {\alpha_l}^2} \tag{4.33}$$

and so on. Thus, we can express the conductivity in terms of the edge level as

$$K_m^N = \frac{\pi (r_1 {\alpha_r}^{m-1})^4}{8\mu l_1 {\alpha_l}^{m-1}} \qquad m = 1,2,...,M \tag{4.34}$$

Now, the pressure drop between any two nodes at different arbitrary chosen levels L_a and L_b is found by summing Equation (4.30) over all bifurcation points between this node and the root node, yielding

$$p_a - p_b = \sum_{i=a+1}^{b} (K_i^N)^{-1} q_i = (\kappa_{a,b}^N)^{-1} q_1 \qquad a,b = 0,1,2,...,M \tag{4.35}$$

where

$$\kappa_{a,b}^N = \left(\frac{8\mu l_1}{\pi r_1^4} \sum_{i=a}^{b-1} \frac{\alpha_l^i}{2^i \alpha_r^{4i}} \right)^{-1}. \tag{4.36}$$

Now we can express the pressure difference between the chosen macro terminal node $p_{M'}$ and the micro terminal node p_M in terms of Equations (4.35)-(4.36):

$$p_{M'} - p_M = (\kappa_{M',M}^N)^{-1} q_1 \tag{4.37}$$

Finally, we need an expression for the cell area. Here, the initial configuration data has been chosen such that the area of the cells are all equal and given by the following:

$$A_\omega = \frac{A_\Omega}{2^{M-1}} \tag{4.38}$$

Now we insert into the equation for K^T:

$$\begin{aligned} K^T &= \frac{q_M}{(p_{M'} - p_M)A_\omega} \\ &= \frac{\frac{q_1}{2^{M-1}}}{(p_{M'} - p_M)\frac{A_\Omega}{2^{M-1}}} \\ &= \frac{\kappa^N_{M',M}}{A_\Omega} \end{aligned} \tag{4.39}$$

And hence,

$$K^T := \left(A_\Omega \frac{8\mu l_1}{\pi r_1^4} \sum_{i=M'}^{M-1} \frac{\alpha_l^i}{2^i \alpha_r^{4i}} \right)^{-1} \tag{4.40}$$

4.4.4 Verifying the coarse approximation

To verify the coarse approximation, we check that the two models are equal when we remove only one level of the tree. For this method of verification, we leave the Peaceman correction out of the reference model, since this will introduce a small error in the coarse approximation. The pressure in the terminal node is then equal to the pressure in the cell in this test case.

Cutting away only one level, we have $L_{M'} = L_M - 1$, and we get, by Equation (4.40), that

$$K^T = \frac{\pi (r_1 {\alpha_r}^{M-1})^4}{8\mu l_1 {\alpha_l}^{M-1}} \frac{2^{M-1}}{A_\Omega} = \frac{K^N_{M'}}{A_\omega} \tag{4.41}$$

and, consequently,

$$q^T = -K^T(p^D - p^N_{M'}) = -\frac{K^N_{M-2}}{A_\omega}(p^N_M - p^N_{M'}) = \frac{q^N_{M'}}{A_\omega}$$

This holds because we leave out the Peaceman correction and $p^D = p^N_M$. Now, replacing K^T with $\frac{K^N_{M'}}{A_\omega}$, q^T with $\frac{q^N_{M'}}{A_\omega}$ and $\int_{\omega_i} dx$ with A_ω in the system matrix in Section 4.3.2 we obtain the same system matrix as in Section 4.3.1. We verify this by solving for the domain pressure p^D using both models, proving that we obtain the same answer. The error has been calculated using the root mean square (RMS) error divided by the pressure difference in the root node pressure $\mathbf{p}^N_{Dirichlet}$ and the domain boundary pressure $\mathbf{p}^D_{Dirichlet}$:

$$RMS = \sqrt{\frac{\sum_{cells} A_{cell}(p_{ex} - p_{coarse})^2}{A_\Omega}} \tag{4.42}$$

$$e_{rel} = \frac{RMS}{\mathbf{p}^N_{Dirichlet} - \mathbf{p}^D_{Dirichlet}} \tag{4.43}$$

5 Numerical results

In this chapter we present the results achieved through the methods described in Chapter 4. The chapter is structured as follows:

Section 5.1 presents the verification of the TPFA method and of the coupled system, as described Section 4.4.1 and Section 4.4.2, respectively.

In Section 5.2 we present the results from the deterministic tree. This tree serves as a well suited test case due to its symmetric structure, and these results will be used in order to better understand the results from the unstructured networks.

Section 5.3 presents the results on the unstructured networks. Here we do also investigate the hypothesis of a radial dependency of K^T.

Section 5.4 provides a summary of the main results.

5.1 Code verification and validation

5.1.1 Verification of the Two Point Flux Approximation (TPFA) method

Here we present the results from the verification method in section 4.4.1. Figure 5.1 shows that the numerical solution to the testproblem (4.25)-(4.26) obtained with the FV-TPFA method on an irregular Voronoi grid and a dirac type right hand side is close to converge with order 1. The red line is a reference to 1^{st} order convergence. The error $e[kPa \cdot mm]$ was calculated according to Equation (4.27), and $h[mm]$ is the average area of one grid cell, that is $h = \sqrt{\frac{A_\Omega}{n_{cells}}}$. The dashed lines represents the 10 tests that have been done. Recall that the grid is a Voronoi diagram based on the terminal nodes of the graph, and that each "grid refinement" involves the generation of a new random graph with twice as many terminal nodes, which is why each test gives different results.

5.1.2 Verification of the coupled system

The results from the verification method described in Section 4.4.2 is presented in Figure 5.2. As with the test of the FV-TPFA method, 10 tests was done from which the mean error and standard deviation was calculated. Considering the average, we conclude that the method converges with what appears to be about 1st order rate.

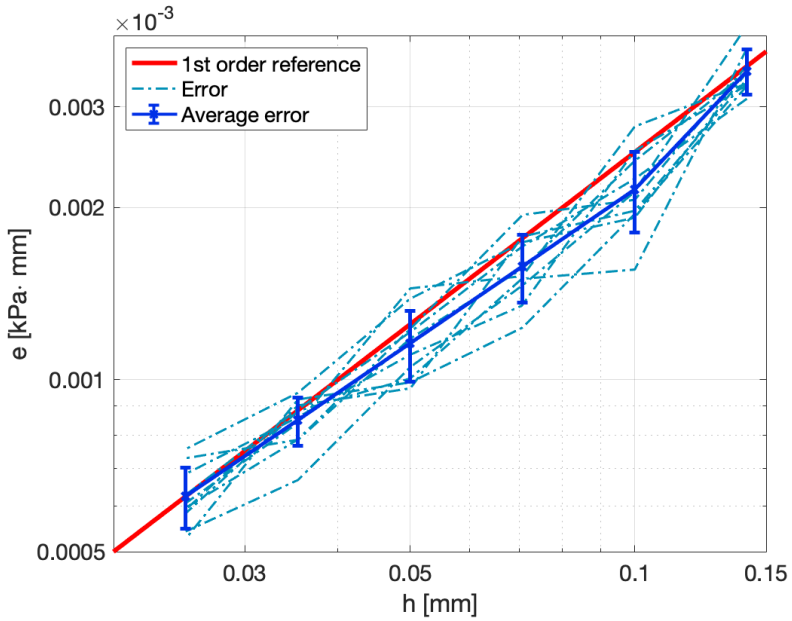

Figure 5.1: *Convergence plot of test case presented in Section 4.4.1. The dashed lines represents the convergence results for each individual test case, while the thick blue line is the average error of all the test cases, with error bars showing the standard deviation. The red line is a reference to exact 1st order convergence, and its intersection point is arbitrary and irrelevant.*

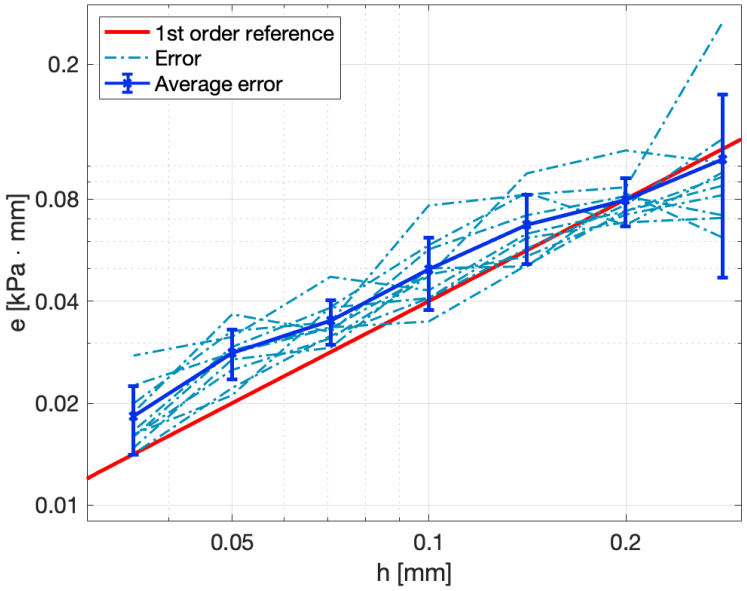

Figure 5.2: *Convergence plot of test case presented in Section 4.4.2. The dashed lines represents the convergence results for each individual test case, while the thick blue line is the average error of all the test cases, with error bars showing the standard deviation. The red line is a reference to exact 1st order convergence.*

5.2 Experiments on the structured network

5.2.1 Verifying the calculations of the transfer conductivity

The calculation of K^T is here validated according to Section 4.4.3 on the deterministic tree. That is, we have compared the analytically calculating values by Equation (4.40) with the numerically calculated value of K^T. We used the following initial configuration: Maximum node level L_8, trunk length of tree $l_1 = \frac{5}{2\sqrt{2}}$ *mm*, length reduction rate $\alpha_l = \frac{1}{\sqrt{2}}$, trunk radius $r_1 = 0.05$ *mm* and radius reduction rate $\alpha_r = 0.7$. This gives terminal edge radii equal to 0.0041 mm and a reasonable ratio between vessel radii and lengths. By letting $\Omega := x \in [0,5], y \in [0, \frac{5}{\sqrt{2}}]$, we obtain a space filling tree with equally sized Voronoi grid cells. Figure 5.3a displays the results. Here, the analytically derived K^T is represented by dashed lines, while the numerically calculated values are represented by dots. R is the radial distance between the macro terminal node at $L_{M'}$ to the micro terminal nodes at L_8 within its impact field, and due to the symmetry of the tree we see no radial dependence on K^T, as expected. The right y-axis gives the level difference $L_M - L_{M'}$.

For $L_M - L_{M'} = 1$, we have two overlapping data points only, as the macro node at L_7 supplies only two cells with equal distance R to both. We have more data points at larger level differences because the macro terminal node then supplies a larger amount of cells. With $L_M - L_{M'} = 8$, the root node is the macro terminal node, and thus the impact field is the whole domain. The impact field of a macro terminal node at L_3 is illustrated in Figure 5.3b.

From Figure 5.3a we do the following observations and reflections:

- K^T is inversely proportional to the level difference $L_M - L_{M'}$. That is, the higher gap between macro and micro terminal node, the lower transfer conductivity.
- The inverse proportionality is explained by the fact that the fluid loses pressure along its flow path due to resistance in edges. By increasing $L_M - L_{M'}$, we consider a longer flow path with higher resistance, over which more pressure is lost, in the calculation of K^T.
- Most pressure will drop over edges with the highest resistance, i.e. the high-level edges with the smallest radii. Therefore we see larger differences between K^T values for lower values of $L_M - L_{M'}$.
- These observations indicates that the conductance in edges over which most pressure drops is a determining factor for the value of K^T.

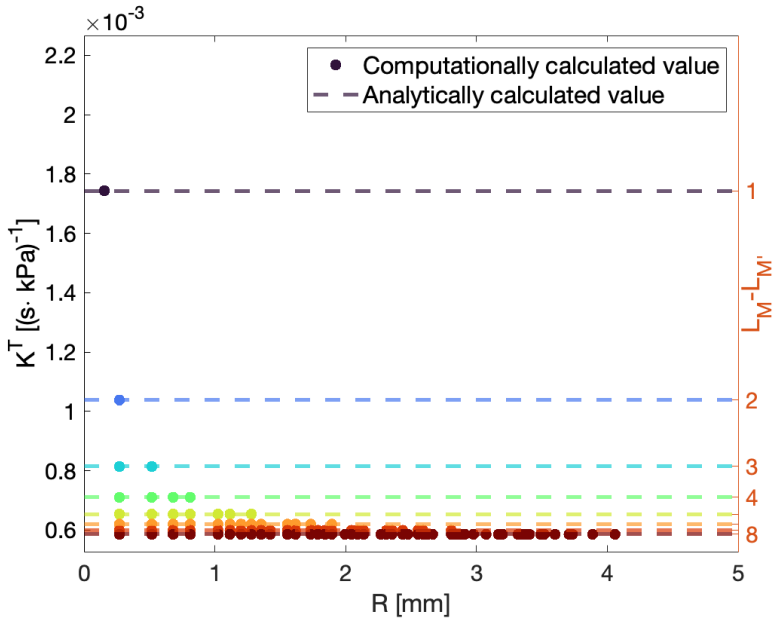

(a) K^T *calculated on a deterministic, space filling tree, both analytically (dashed lines) and computationally (dots). R is the radial distance from the given macro terminal node to the micro terminal nodes. The right y-axis shows the level difference between the macro terminal node and the micro terminal nodes. Different colors are chosen for visual purposes. We have more data points at higher level differences because this corresponds to a bigger impact field, see figure (b).*

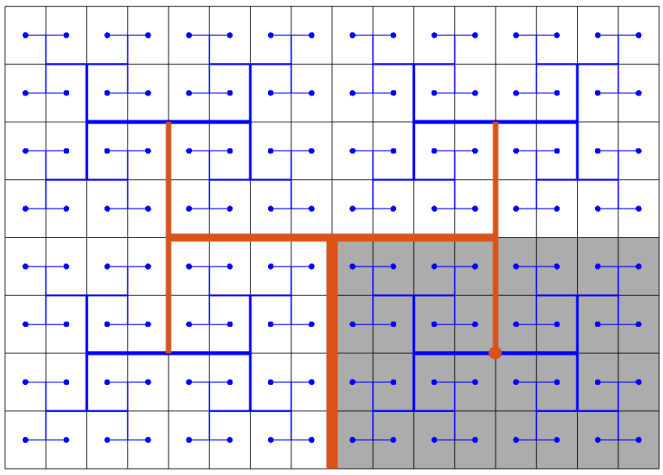

(b) *The impact field of a macro terminal node is the collection of all the cells that are supplied through that node, and is here marked in gray. The visible tree is drawn in red, and the invisible in blue. Here, maximum node level is* L_8 *and the macro terminal node is placed at* L_3 *and marked with a red dot. Note that for each step we move the macro node closer to a micro node, the impact field is halved, so that for* $L_M - L_{M'} = 1$ *the impact field is only two cells, while with* $L_M - L_{M'} = 7$ *the impact field is the whole domain.*

Figure 5.3: *a)* $K^T(R)$ *and b) impact field for a deterministic, symmetric tree. The transfer conductivity with a given macro terminal node is constant, as expected.*

5.2.2 Testing of sensitivity to network variables

In Figure 5.4, we look closer at how the edge radii affects the value of K^T by letting α_r vary from 0.4 to 0.9. Recall that the smaller α_r, the more dramatic reduction in radii for each level jump, and $\alpha_r = 0.4$ means that the radii are more than halved. The results of varying α_r is thus radical differences in the terminal edge radii, and the consequences are clear in the figure: At most, the difference in K^T is of order 10^{10}. A striking observation from the figure is also that the results are practically independent of the level difference for sufficiently small radii. When the radii shrink slowly ($\sim \alpha_r > 0.6$), K^T is also quite dependent on how much of the tree that is removed. This as opposed to when the reduction factor is small and the radii becomes very small very fast ($\sim \alpha_r \leq 0.5$). Then the placement of the macro terminal node plays no role at all.

We may explain these results as follows: When the edge radii are just slightly decreasing, the variation in edge resistance is small (since the edge radius is the most important factor for the resistance). The pressure drop over each edge will therefore be nearly constant, and the pressure in the nodes will decrease almost linearly in the whole flow path. K^T will therefore be more dependent on the placement of the macro terminal node. That as opposed to when the radii shrinks very quickly. The resistance in the flow path will as a result increase dramatically for each level increase. The insignificance of the level difference as α_r decreases indicates that almost all pressure drops over the terminal edges. What we see in the figure is hence that *the more the resistance in terminal edges dominates the pressure profile, the less is the significance of the placement of the macro terminal node for the value* K^T.

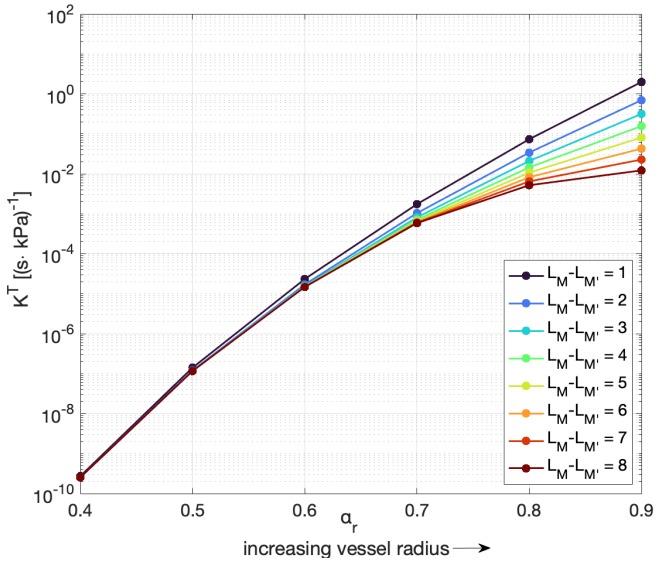

Figure 5.4: *The value of* K^T *is strongly dependent of the vessel radii. Here, the reduction factor* α_r *in radius is varying from 0.4 to 0.9, resulting in a difference of order* 10^{10} *in* K^T *at most. Also, the number of levels removed has practically no influence on* K^T *for low* α_r.

5.2.3 The coarse model approximation

The coarse model was validated according to Section 4.4.4. Six graphs with varying L_M were used as test cases and the error was zero for all.

Test case 1: Identifying important parameters

We want to test how well the coarse model approximates the reference model, the Peaceman correction included (which was left out in the validation). In this section we present the results from investigating which model parameters that affects the results of the approximation the most. We divided the model parameters into three groups:

1. Fixed parameters. This includes structure parameters that results in the wanted graph structure, namely a tree yielding equally sized Voronoi cells which is space filling for a sufficient amount of levels. We fixed the domain $\Omega := x \in [0,5], y \in [0, \frac{5}{\sqrt{2}}]$, the root length $l_1 = 0.05\ mm$, the length reduction factor $\alpha_l = \frac{5}{2\sqrt{2}}$, and the bifurcation angle θ at 90°. Also, we kept the viscosity μ constant at $3 \cdot 10^{-6}\ kPa \cdot s$ and assumed this to be the "true" blood viscosity.

2. Structural parameters. We investigate how the error depends on the network complexity, i.e., the maximum level L_M, and how much of the graph we remove in the approximation, i.e. the level difference $L_M - L_{M'}$.

3. Conductivity parameters, that is, parameters affecting the conductivity in the domain and the network. In the domain we vary K^D by varying the permeability k, assumed to be isotropic. $k = 3 \cdot 10^{-5}\ mm$ was used as reference value as this has been used as a physical parameter in related literature. This gives $K^D = 10\ \frac{mm^2}{s \cdot kPa}$. The network conductivity K^N is varied through the radius reduction factor α_r.

Hence, four model parameters were considered: L_M, $L_M - L_{M'}$, K^D and α_r. In Figures 5.5 we present the results as the error in the domain pressure $\mathbf{p}^D$ according to Equation (4.43) as function of the various parameters. In each test, two parameters were fixed and two others varied.

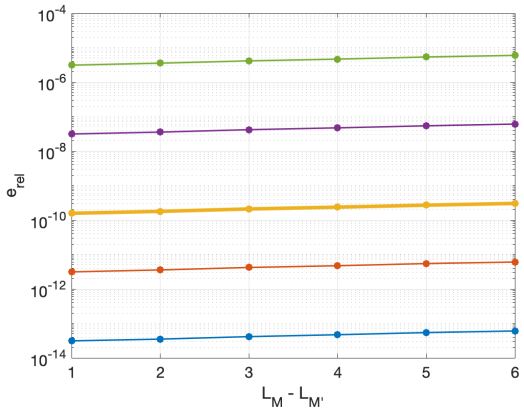

(a) Fixed: $M = 8$ and $\alpha_r = 0.7$.
Varying: K^D and $L_M - L_{M'}$.

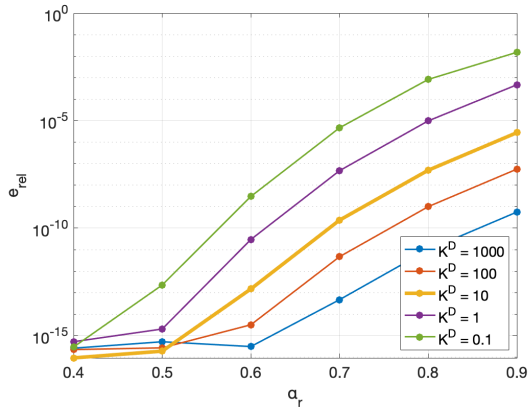

(b) Fixed: $M = 8$ and $L_M - L_{M'} = 4$.
Varying: α_r and K^D.

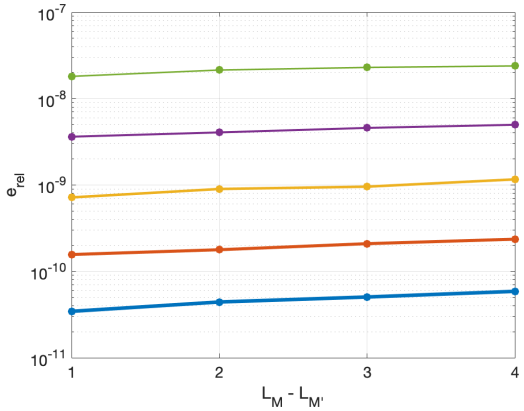

(c) Fixed: $\alpha_r = 0.7$ and $K^D = 10\frac{mm^2}{s \cdot kPa}$.
Varying: M and $L_M - L_{M'}$.

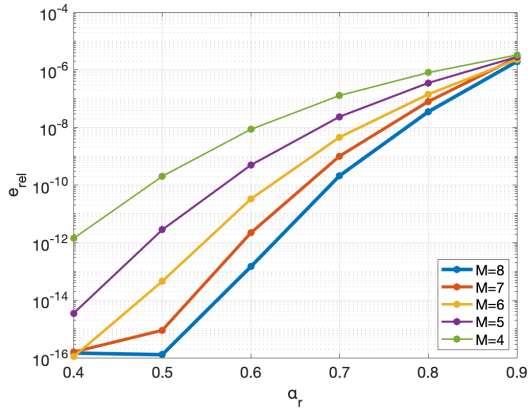

(d) Fixed: $K^D = 10\frac{mm^2}{s \cdot kPa}$ and $L_M - L_{M'} = 3$.
Varying: M and α_r.

Figure 5.5: *Here we test the sensitivity of the coarse approximation to four different variables: α_r is the radius reduction factor, K^D is the domain conductivity, M is the maximum level in the tree and $L_M - L_{M'}$ is the level difference between the macro and micro terminal node. The tests are done by fixing two variables and letting the two others vary. The legend in (b) also accounts for (a), and the reference value $K^D = 10\ \frac{mm^2}{s \cdot kPa}$ is marked with a thicker, yellow line. Similarly, the legend in (d) also accounts for (c). Note that the axis limits are varying. On these plots we have several datapoints where $e_{rel} < 10^{-15}$, which is in the range of machine precision and thus interpreted as zero.*

Figure 5.5a shows that, for all K^D values, increasing level difference results in a bigger error. This is expected, as increasing level difference means that we remove a bigger part of the network, and by that more information about the flow details. However, the level difference is by far not as important as the value of the domain conductivity K^D, and for the highest value of K^D the error is close to zero even when we remove 6 out of 8 levels of the tree. The figure indicates that *the error is more influenced by conductivity parameters than structural parameters*.

Looking at 5.5b we see that α_r also has a dramatic impact on the results, and significantly more than the

level difference, which was here kept constant. Recall that low values of α_r means that the radii reduces quickly, and notice that for $\alpha_r = 0.4$, the error is (numerically) zero also for low K^D values. However, here the error increases immediately as we increase α_r, while for high K^D we can allow a bigger reduction rate before we see any increase. Lower α_r results in lower transfer conductivity, as seen in Section 5.2.2. Since small α_r entails narrow terminal edges dominating the pressure profile, this indicates that *lower errors are obtained with more pressure drop in the network, and less in the domain.*

The results in Figure 5.5c and Figure 5.5d may be explain in light of these insights. Both figures reveal that a higher network complexity results in lower error, which at first might seem unreasonable as it should be easier to approximate something less complex. However, a more complex network yields higher network resistance, as the edge radii decreases for each level increase. Thus, with higher complexity, more pressure drops over the network. The results in (d) is particularly interesting: For large α_r, the network edges shrink just slightly for each level increase, and whether there are 4 or 9 levels does not significantly impact how much pressure that drops over the network. However, for low α_r, the difference between 4 and 9 levels has a dramatic impact on the terminal edge radii, and, correspondingly, for the pressure differences in the network. Thus, it seems like *the network complexity is only important for the error if network parameters (such as radii) varies significantly with varying complexity.*

To explain the sensitivity to conductivity parameters, we must recall that flow in this model regime will always search for the most effective flow path towards the minimum pressure at $\partial\omega$. Thus, for sufficiently low K^D compared to K^N, it becomes more efficient to reach the boundary through the network terminal edges, and the network flow is altered by the pressure gradients in the domain. This flow pattern is not captured in the coarse model, as the network is removed and replaced by a linear flow model unable to replicate such effects. From Figure 5.6b) we also note the pressure difference between terminal edges and the domain due to the Peaceman correction (see Equation (4.18)), which increases as we increase the domain conductivity. This pressure drop is neither accounted for in the coarse approximation. Thus, *both the effects of altered network flow and of the Peaceman correction are not captured by the coarse approximation and results in higher errors for higher pressure gradients in the porous domain.*

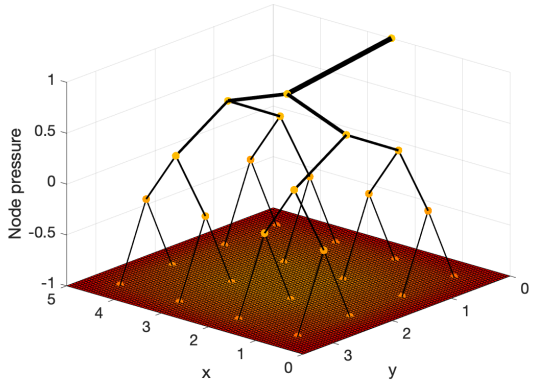

(a) *Pressure plot for the reference model with* $K^D = 1000\,\frac{mm^2}{s \cdot kPa}$. *Network setup as in Section 5.2.1, but with maximum level* L_5.

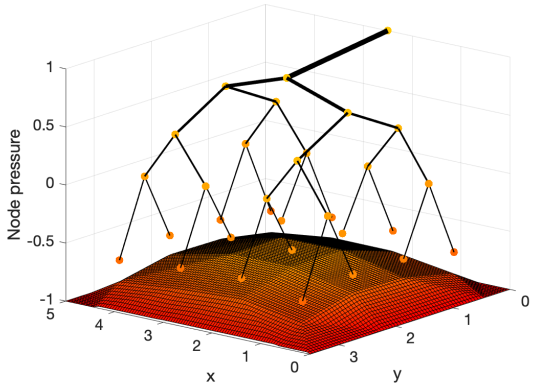

(b) *Pressure plot for the reference model with* $K^D = 0.1\,\frac{mm^2}{s \cdot kPa}$. *Otherwise same setup as in (a).*

Figure 5.6: *(a): When* K^D *is high and the resistance to flow is lower in the domain than in the network, most pressure drops over the network. (b): For high* K^D*, the pressure gradients in the domain are larger, and that the Peaceman correction (seen as the gap between terminal nodes and the domain) becomes more important for the pressure profile. The error in the coarse model is higher in case (b).*

Test case 2: Fixed radius setup

Before proceeding to the unstructured networks, we consider one final test case where we use the setup for the radii described in Section 4.1.2 (used for the unstructured networks), where we fix the radius of the root edge and the terminal edges. Thus, we test how the results vary when one of the most important conductivity related parameters, i.e. the smallest radius in the network, is fixed. r_R was set to 0.5 mm as this is approximately the size of the smallest radii visible in medical pictures. r_T was set to typical capillary radii of 0.004 mm. We cut the tree at L_1 and varied the maximum level L_M to observe the effect of varying network complexity. The resulting K^T values and the error in the coarse approximation are displayed in Figure 5.7.

Figure 5.7a shows that by fixing the terminal edge radii, we do not get the same variations of several orders in the results. The variations we see is now due to variations in terminal edge length, which is reduced by a factor α_l for each level increase. The results of the coarse approximation with this setup and different K^D values is shown in 5.7b. K^T is increasing with increasing M, and the error is correspondingly increasing, since higher network conductivity results in smaller pressure drop over the network. The important message from this test case is that the order of K^T seems to be highly dependent of the terminal edge radii, as the variations in K^T is much smaller when they are kept fixed. However, these results elucidate that the effect of edge length is not negligible, and that*the conductivity of single graph edges, which depends both on edge radii and length, are important for the value of* K^T.

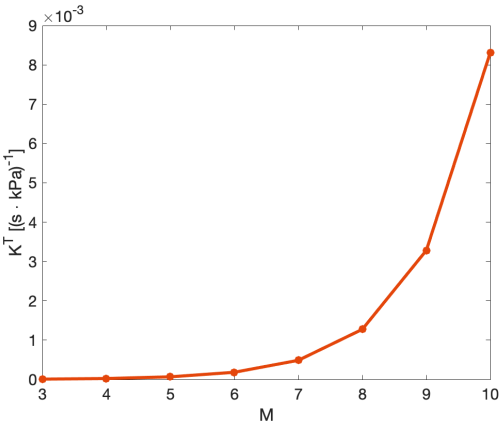

(a) K^T *measured on a tree with the radius setup described in Section 4.1.2. The macro terminal node is kept at* L_1 *and the maximum level* L_M *is varied.*

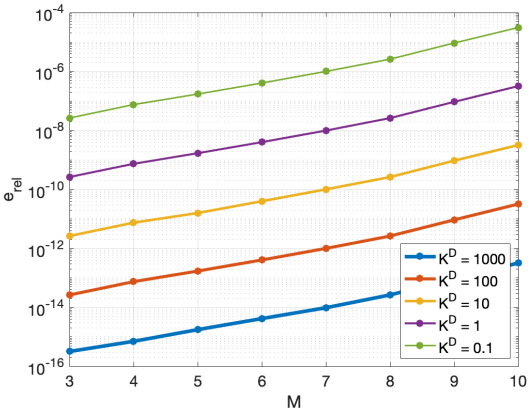

(b) *The coarse approximation with the* K^T *values found in (a) for different values of the domain conductivity* K^D.

Figure 5.7: *Test case with constant terminal edge radii and varying complexity.*

5.3 Results on unstructured networks

The results for the DLA generated network and the rapidly-exploring random tree are now presented. Model parameters are set as follows: We fix the domain $\Omega := x, y \in [0,1]$ and use the radius setup described in Section 4.1.2 with $r_R = 0.5$ mm and $r_T = 0.004$ mm as in the final part of the last section. We then look at how the transfer function K^T and the coarse approximation depends on the complexity of the network. For the DLA generated network, we indicate its complexity by referring to the number of particles that is involved in its generation. More particles leads to higher complexity, and it will also lead to more terminal nodes, but there is no exact connection between the two. However, it is noted that twice as many particles gives approximately twice as many terminal nodes, and 16 000 particles, which is the most complex network we will use herein, corresponds to $\sim$ 1000 terminal nodes. The number of terminal nodes will be used to indicate the complexity of the rapidly-exploring random tree. Since both networks has terminal nodes at different levels, we will always use the root node at L_0 as macro terminal node. Thus, we measure K^T as a parameter for the entire network, and the coarse model is an approximation of the entire network. This means that the pressure difference when calculating K^T is always the same, and variations in K^T values are due to other factors.

5.3.1 The transfer function on DLA generated network

Figure 5.8 shows two DLA generated networks of different complexity and a color map of K^T where lighter colors indicates higher values. Note that when adding more particles, the network grows outwards from the root and covers a larger share of the domain. The network develops a few main branches that splits into progressively thinner branches. Considering the K^T values, the pattern is clear, especially for

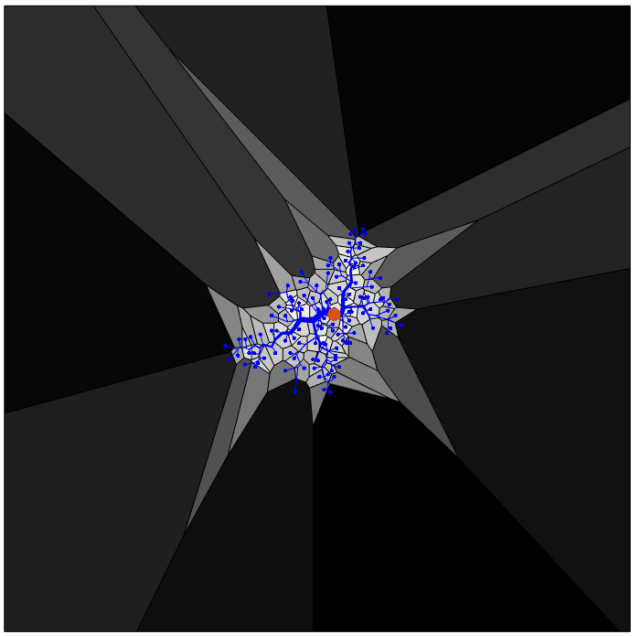

(a) *DLA tree generated with 2000 particles.*

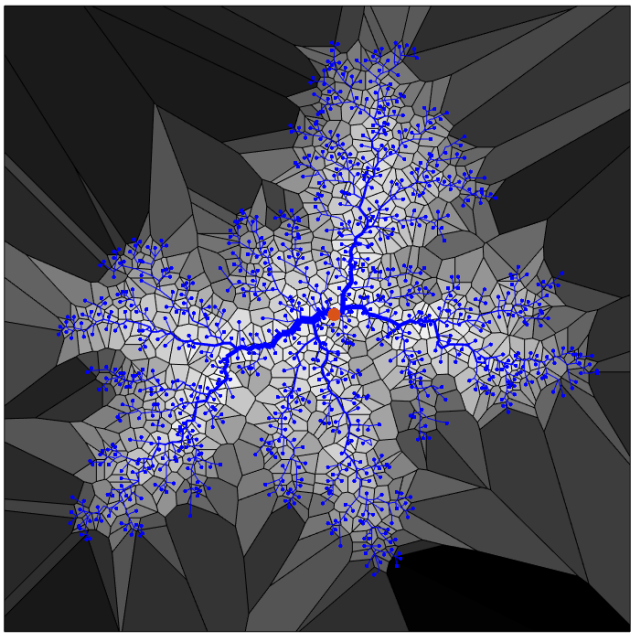

(b) *DLA tree generated with 16000 particles.*

Figure 5.8: *Two DLA generated networks of different complexity together with a color map of the K^T value for each micro terminal node. Light colors indicates higher values. The red dot represents the macro terminal node, and the blue dots represent micro terminal nodes.*

the bigger network: *Higher values gather around the main branches near the root, while the lowest are found at the outer most terminal nodes.*

In order to investigate the modelling assumption about the flow distribution being inversely proportional to radial distance, we have plotted $log_{10}(K^T)$ as a function of R at four different network complexities, see Figure 5.9a. R is the distance between the macro terminal node and each micro terminal node. We did a linear approximation from the data points, and used the slope coefficient as an indication of the R-dependence, which are plotted in Figure 5.9b. As the trees are randomly generated, we based each regression model on 10 different trees at each level of complexity. The slope is negative for all networks, and in all cases we found that the p-value of the slope coefficient is < 0.05, meaning that *the spatial dependency is statistically significant*. The R^2 values ranges from 0.159 for the network with 1000 particles to 0.309 for the network with 16 000 particles. This indicates that as the complexity increases and the network fills up more of the space, the overall spread in K^T values decreases.

The variations we see in K^T is the result of variations in flow in terminal edges, which in turn is the result of some flow paths being more efficient than others. Both the length of a flow path and the resistance in each edge determines the resulting terminal edge flow. The flow in edges directly linked to the main branches will therefore be higher, while for distant terminal edges at the sub-branches, the fluid loses more pressure along the path, and the terminal edge flow is lower. For this network, we note that *the path length and radial distance R to terminal nodes are to a large extent coinciding, and therefore, K^T shows a tendency to be a decreasing function of R.*

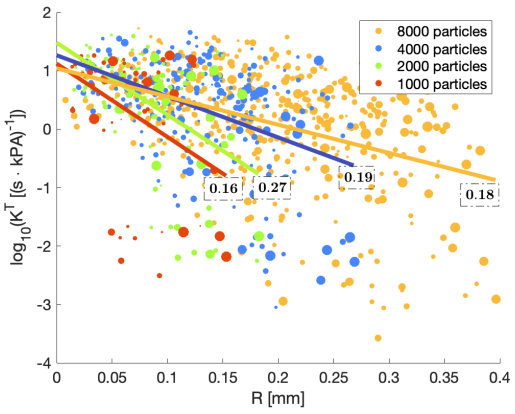

(a) *We have plotted $log_{10}K^T(R)$ and the linear regression model on four networks of different complexity. "Particles" refer to the way the tree is generated, but the data points represent terminal nodes. The marker size reflects the area of the distribution region of the terminal node. The R^2-value of the model based on 10 networks is plotted at each graph. The network of 16000 particles having $R^2 = 0.31$ is not plotted for visual purposes.*

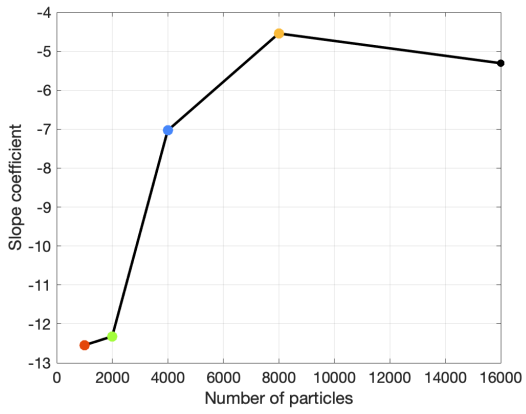

(b) *Here we plot the slope coefficient from the linear regression model for trees of varying complexity. Each data point is based on data from 10 different trees, in which one of them is plotted i (a) with the same color as the corresponding data point. Here we have also included trees with 16 000 particles, but this is not plotted in (a) due to visual purposes.*

Figure 5.9: *We investigate the modelling assumption about the flow distribution being inversely proportional to the distance R from the macro to micro terminal node. The p-value of the slope coefficient was found to be < 0.05, hence, the spatial dependency is statistically significant.*

5.3.2 The transfer function on rapidly-exploring random tree

Figure 5.11 shows two trees of different complexity, and note that even with a relatively low complexity, the branches reaches out to cover outer parts of the domain as well, and the network grows denser as the complexity increases. As for the DLA network, the highest values are gathered around the main branches. Low values are found at areas with a long path distance from the root, but as opposed to the DLA network, *this does not necessarily correspond to a long radial distance*. For instance, the black spot a little to the right of the root node in Figure 5.11b is very close in radial distance, but far if we consider the path from the root node. However, what seems to be common for both the unstructured networks is that the terminal edges near the root, especially the short ones, dominates the flow. This in addition to variations due to path length, is most likely the reason behind the K^T distribution pattern we see here for both unstructured networks.

The distribution pattern of K^T in Figure 5.11 is reflected in Figure 5.10a, in the sense that high and low K^T values are found at the same radial distances. A linear approximation to $log_{10}(K^T)$ is clearly a bad fit, with R^2 values (not displayed in the figure) varying between 0.018 and 0.054. However, the slope coefficients, plotted in Figure 5.10b have p-values < 0.05, thus, *the radial dependence is statistically significant*. The increasing slope of the linear regression model of $log_{10}(K^T)$ at higher complexity may be explained by the fact that a new terminal edge linked to a main branch will significantly alter the flow and lead to a larger gap between the K^T extremities. This happens as a result of the space-filling algorithm, allowing new nodes to appear at any empty space in the domain, near the root as likely as in the periphery.

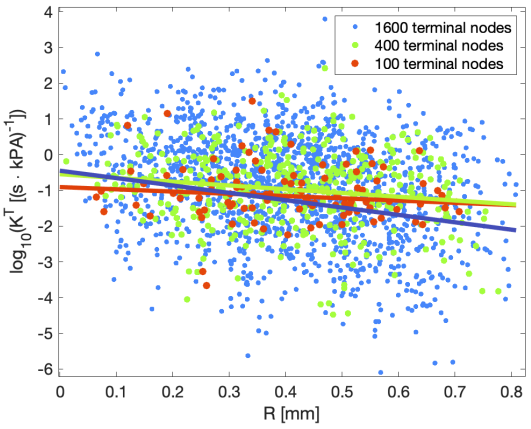

(a) *Linear regression approximation of K^T as a function of the distance R between the macro and micro terminal node on three different rapidly-exploring random trees. An increase in the number of terminal nodes results in a denser tree with many short edges, which seems to result in a larger spread in the K^T values. The R^2-values, alternating between 0.018 and 0.054, has been left out of the plot for visual purposes.*

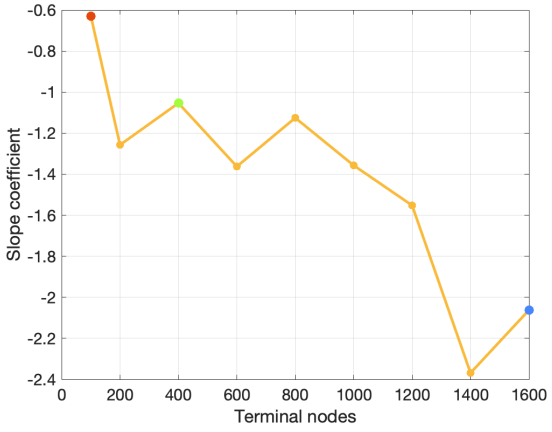

(b) *The slope coefficient of the linear regression approximation as a function of the number of terminal nodes. Each data point is based on the data from 10 different trees. The red, green and blue data points thus represent the data points in (a) except that these points are from one single tree.*

Figure 5.10: *Analogous to Figure 5.9.*

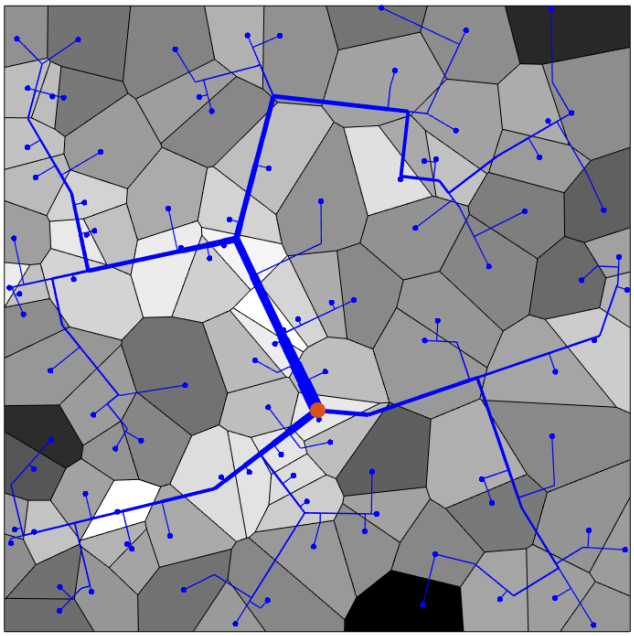

(a) *Rapidly-exploring random tree with 100 terminal nodes.*

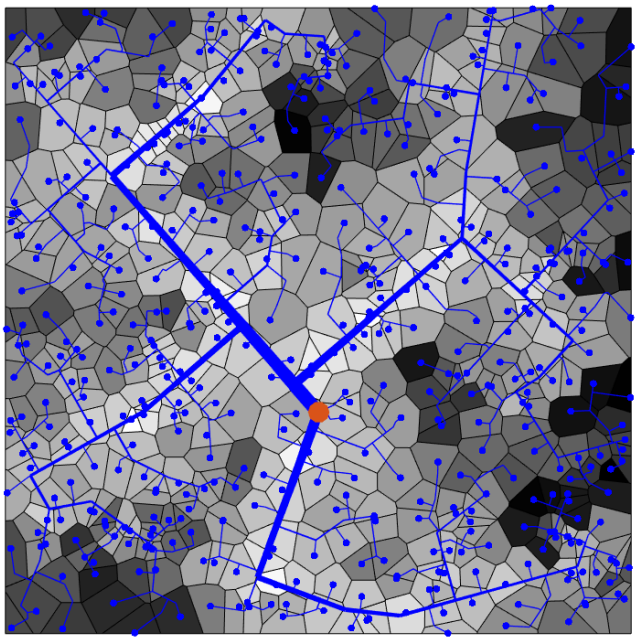

(b) *Rapidly-exploring random tree with 500 terminal nodes*

Figure 5.11: *Analogous to Figure 5.8. Lighter colors indicates higher* K^T *values.*

5.3.3 Coarse model approximation

Finally, we look at the results of a coarse approximation of the unstructured trees. For the approximation we used the K^T value from the linear regression model of $log_{10}(K^T(R))$ found in the previous section. That is, we used the coefficients in Figure 5.9b and Figure 5.10b and the corresponding intercept coefficients. Hence, $K^T(R) = 10^{slope \cdot R + intercept}$. We calculated the average error and the standard deviation on the basis of 10 networks for each test. As in Section 5.2.3, the error was measured in the domain pressure $\mathbf{p}^D$ calculated with the reference and the coarse model according to Equation (4.43).

The results for the DLA generated network and the RRT are displayed in Figure 5.12a and 5.12b, respectively. The legend in Figure 5.12b accounts for both figures. The errors are here many magnitudes bigger than those for the deterministic tree, which is expected as we use approximated K^T values. However, despite that many of the data points deviated from the linear regression model, especially for the RRT, the errors may be considered small. For $K^D \leq 10 \frac{mm^2}{s \cdot kPa}$, which was our reference conductivity value, errors remains below 1% for both networks. The range of e_{rel} is about the same for both networks, with a slightly larger standard deviation of the error at the RRT. We still conclude that the differences are, a bit surprisingly, not very large. It thus seems like *as long as the conductivity parameters results in that most pressure drop happens in the network, the network structure plays a minor role on the results of a coarse approximation*.

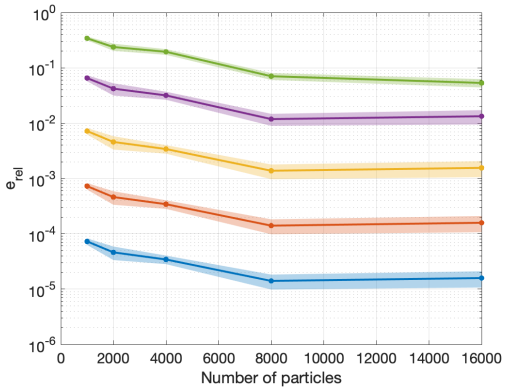

(a) *The relative error in domain pressure between the reference and coarse approximation on DLA generated trees of varying complexity for different K^D values. Each data point is based on data from 10 different trees. The dashed-dotted line is the mean error and the shaded area shows the standard deviation.*

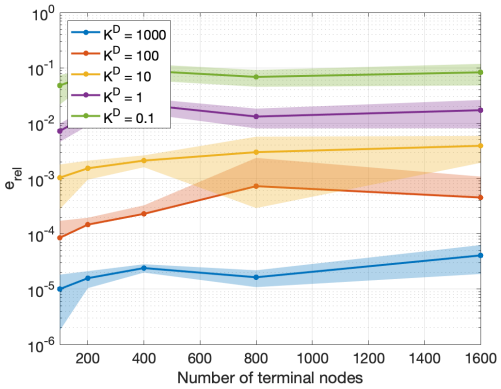

(b) *Analogous to (a), but for the rapidly-exploring random tree. For the red graph ($K^D = 100$), some of the standard deviation values $std(e_{rel})$ was greater than the mean value, and in order to use the logarithmic axis scaling we have plotted the deviation above the graph only.*

Figure 5.12: *Relative error in domain pressure $\mathbf{p}^D$ calculated with the reference and the coarse model for a) the DLA generated network and b) the rapidly-exploring random tree.*

5.4 Summary

Through the numerical experiments we have investigated the distribution of K^T for three different networks, and whether a coarse approximation of these networks in terms of K^T is a valid approximation. Using the deterministic tree as a perspicuous tool to understand the influence of isolated variables, and the unstructured trees as "biological-like" test cases, we can summarize the results as follows:

- K^T, which may be considered as the total conductivity for a given flow path in a network, is highly dependent on the conductivity of single graph edges as well as the flow path length.
- K^T tends to decrease with increasing distance R from macro to micro terminal node when the length of the flow path is associated with higher values of R. This tendency is clearer for the DLA generated network than for the rapidly-exploring random tree.
- The error in the coarse model approximation is small when most pressure is lost in the network and the pressure gradients in the domain are small. Large pressure gradients in the domain result in higher error in the coarse approximation, leading to alterations in the network flow also affecting the Peaceman correction that the linear flow model is unable to replicate.
- The error therefore depends more on the conductivity parameters (K^D, K^N) than on network structure and complexity.

6 Discussion and conclusions

We will here discuss the main results summarized in Section 5.4. First, if the vessel network resembles any of the unstructured networks, the flow distribution may exhibit a radial dependency (in terms of distance from the macro terminal), and the flow from a feeding artery into the tissue can be modelled with a finite support area. This eliminates the need for a full network-domain connectivity in a model, and the calculations thus simplify considerably. The appropriate functional relationship between K^T and R remains however an open question, and will most likely depend on the network structure. Secondly, our results indicate that the coarse model may be suitable for coupled problems where most pressure is lost in the network, while pressure gradients in the domain are small. The small errors for the unstructured networks indicate model robustness. However, it also underlines the importance of an appropriate pressure distribution for the validity of the model. In vascular networks, most pressure is lost over arterioles and venules (Formaggia et al., 2010) and not in the capillaries. According to our results, the K^T parameter should hence incorporate arterioles and venules for a coarse model to be valid for blood flow simulations. Moreover, there is reason to believe that an extended model with a corresponding venous compartment will allow for higher pressure gradients in the porous domain. The effect of internal sinks in the form of venules is expected to result in less flow across the domain, and, consequently, less alterations in the network flow. Our claim is therefore that the coarse model may be sufficiently accurate for modelling purposes using a two-compartment model. Finally, the fact that K^T is highly dependent on vessel radius distributions implies a sensitivity to changes in the structural morphology of a vessel network. This indicates that the transfer conductivity may be used as a biological marker for diagnostic purposes, as many medical conditions involve morphological alterations. By inverse modelling, *in vivo* measurements of K^T may be feasible with an initial value obtained from a realistic synthetic network. We therefore conclude that our results are interesting both from a modelling but also potentially from a clinical perspective.

A natural discussion point is to what extent our networks are comparable to real vessel networks. Based on the suggestion by Fleury and Schwartz (1999) about vascular formation being governed by a Laplacian growth mechanism, we may assume that the DLA network is the most physiologically relevant network considered herein. A natural prolongation of this work is to test our methodology on synthesized but realistic networks, e.g. obtained from a CCO method as in Schreiner et al. (2006) or from a mouse brain image-based Circulatory Network Synthesis (iCNS) developed by Linninger et al. (2019). Ongoing work on *in silico* based mouse brain network models faces several technical challenges, but discrete graph structures have been obtained using machine learning analysis (Todorov et al., 2020). Such a fully resolved network is valuable for parameter estimations (for instance the transfer conductivity) and provides a true network reference. However, the computational costs associated with fully resolved network models highlights the relevance of coarse approximations.

Our results on a simplified, idealized arterial flow model should encourage to further work towards a realistic global model. First, a corresponding model for the venous compartment needs to be coupled onto this model to be used in a full-brain simulation. As mentioned, this will probably result in a different flow behavior in the domain, and the effect on the error in the coarse model should be investigated. Second, the radius dependence of K^T and the self-regulating mechanisms of the vessel system, controlled by contraction and widening of vessel radii (Formaggia et al., 2010), suggest that a realistic model should incorporate physiological function as well as design. The flow in macro scale vessels should include effects of vessel wall elasticity and the resulting non-linear flow behavior as in Qohar et al. (2021), and a corresponding extensions of the transfer flow model should also be subjected to research.

Several naturally occurring networks are highly hierarchical and appear fractal, and we devote this last paragraph to speculate on possible applications to other types of biological networks with potential gradient driven flow. A captivating analogy is the vascular system of plants, as they as well are live organisms having nutrients transported through a pressure driven transport system. Like the mammalian vascular system, it has two main compartments: the xylem and the phloem, for which coupled models have been built in order to understand function-structure relationships (Hölttä et al., 2009). These relationships are also shown to change due to plant sickness (Brodersen & McElrone, 2013), thus, it is not beyond belief that a coarse model could be used as a tool for e.g. estimating global effects of embolism. River ramifications are another typical example of naturally arising fractal structures. We may consider the landscape in Figure 6.1 as an upside-down version of our reference model, where the porous domain is the impact fields around the stream sources, and instead of diverging branches we have streams that

Figure 6.1: *River ramifications from the Missisippi river. Redistributed from https://www.wikiwand.com/no/Hovedelv#Media/Fil:Mississippiriver-new-01.png, with licence: CCBY-SA4.0.*

progressively widen and join into larger rivers before converging into the main river and flowing into the ocean. It is certainly a time for being concerned about consequences related to changes in water levels, amount of precipitation etc., and modelling complex systems over domains the size of a large country do most likely call for a coarsening.

A Code verification

A.1 Verification of the Two Point Flux Approximation (TPFA) method

A.1.1 Convergence on squared grid

u^h is approximated on each cell with diameter $h = \sqrt{dx^2 + dy^2}$, and the exact value is calculated in the cell center. The error is measured in the L^2-norm, that is, Equation 4.27. On a regular, squared grid, the method is shown to converge with order 2, see figure A.1.

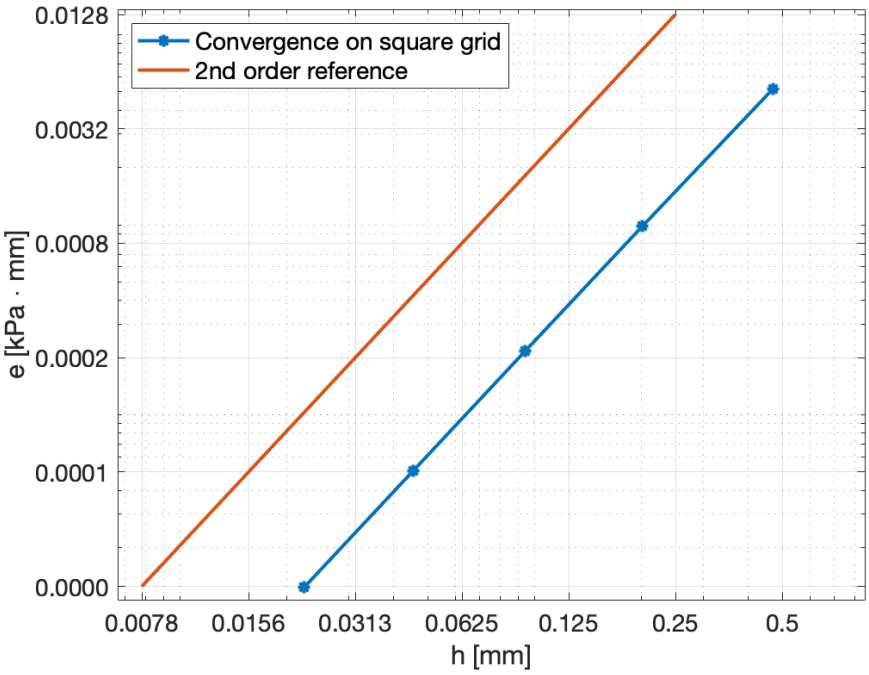

Figure A.1: *Convergence plot of the test problem on a squared grid. h is the diagonal of one grid cell and the error is measured in the L^2-norm.*

Bibliography

Adams, R. A., & Essex, C. (2013). *Calculus: A Complete Course* (8th edition). Prentice Hall Canada.

Blunt, M. J., Jackson, M. D., Piri, M., & Valvatne, P. H. (2002). Detailed physics, predictive capabilities and macroscopic consequences for pore-network models of multiphase flow. *Advances in Water Resources*, *25*(8), 1069–1089. https://doi.org/10.1016/S0309-1708(02)00049-0

Brodersen, C., & McElrone, A. (2013). Maintenance of xylem Network Transport Capacity: A Review of Embolism Repair in Vascular Plants. *Frontiers in Plant Science*, *4*. Retrieved November 14, 2022, from https://www.frontiersin.org/articles/10.3389/fpls.2013.00108

Burch, M., & Weiskopf, D. (2013). The aesthetics of rapidly-exploring random trees. *Proceedings of the Symposium on Computational Aesthetics*, 45–52. https://doi.org/10.1145/2487276.2487285

Chen, Y., Wolk, D. A., Reddin, J. S., Korczykowski, M., Martinez, P. M., Musiek, E. S., Newberg, A. B., Julin, P., Arnold, S. E., Greenberg, J. H., & Detre, J. A. (2011). Voxel-level comparison of arterial spin-labeled perfusion MRI and FDG-PET in Alzheimer disease. *Neurology*, *77*(22), 1977–1985. https://doi.org/10.1212/WNL.0b013e31823a0ef7

Cookson, A. N., Lee, J., Michler, C., Chabiniok, R., Hyde, E., Nordsletten, D., & Smith, N. P. (2014). A spatially-distributed computational model to quantify behaviour of contrast agents in MR perfusion imaging. *Medical Image Analysis*, *18*(7), 1200–1216. https://doi.org/10.1016/j.media.2014.07.002

Darcy, H. (1856). *Les fontaines publiques de la ville de Dijon: Exposition et application des principes à suivre et des formules à employer dans les questions de distribution d'eau, ouvrage terminé par un appendice relatif aux fournitures d'eau de plusieurs villes au filtrage des eaux et à la fabrication des tuyaux de fonte, de plomb, de tole et de bitume*. Victor Dalmont.

Dullien, F. A. L. (1979). *Porous Media: Fluid Transport and Pore Structure*. Academic Press.

Fåhræus, R., & Lindqvist, T. (1931). THE VISCOSITY OF THE BLOOD IN NARROW CAPILLARY TUBES. *American Journal of Physiology-Legacy Content*, *96*(3), 562–568. https://doi.org/10.1152/ajplegacy.1931.96.3.562

Fatt, I. (1956). The Network Model of Porous Media. *Transactions of the AIME*, *207*(01), 144–181. https://doi.org/10.2118/574-G

Fleury, V., & Schwartz, L. (1999). Diffusion limited aggregation from shear stress as a simple model of vasculogenesis. *Fractals*, *07*(01), 33–39. https://doi.org/10.1142/S0218348X99000050

Formaggia, L., Quarteroni, A., & Veneziani, A. (2010). *Cardiovascular Mathematics: Modeling and simulation of the circulatory system*. Springer Science & Business Media.

Gordon, Y., Partovi, S., Müller-Eschner, M., Amarteifio, E., Bäuerle, T., Weber, M.-A., Kauczor, H.-U., & Rengier, F. (2014). Dynamic contrast-enhanced magnetic resonance imaging: Fundamentals and application to the evaluation of the peripheral perfusion. *Cardiovascular Diagnosis and Therapy*, *4*(2), 147–164. https://doi.org/10.3978/j.issn.2223-3652.2014.03.01

Greenfield, J. C., & Patel, D. J. (1962). Relation Between Pressure and Diameter in the Ascending Aorta of Man. *Circulation Research*, *10*(5), 778–781. https://doi.org/10.1161/01.RES.10.5.778

Hodneland, E., Hanson, E., Sævareid, O., Nævdal, G., Lundervold, A., Šoltészová, V., Munthe-Kaas, A. Z., Deistung, A., Reichenbach, J. R., & Nordbotten, J. M. (2019). A new framework for assessing subject-specific whole brain circulation and perfusion using MRI-based measurements and a multi-scale continuous flow model. *PLOS Computational Biology*, *15*(6), 1–31. https://doi.org/10.1371/journal.pcbi.1007073

Hodneland, E., Hu, X., & Nordbotten, J. M. (2021). Well-Posedness and Discretization for a Class of Models for Mixed-Dimensional Problems with High-Dimensional Gap. *SIAM Journal on Applied Mathematics*, *81*(5), 2218–2245. https://doi.org/10.1137/20M1362541

Hölttä, T., Mencuccini, M., & Nikinmaa, E. (2009). Linking phloem function to structure: Analysis with a coupled xylem–phloem transport model. *Journal of Theoretical Biology*, *259*(2), 325–337. https://doi.org/10.1016/j.jtbi.2009.03.039

Huinink, H., Arends, T., & Ruijten, P. (2016). *Fluids in porous media: Transport and phase changes*. Morgan & Claypool Publishers.

Kamiya, A., & Togawa, T. (1972). Optimal branching structure of the vascular tree. *The bulletin of mathematical biophysics*, *34*(4), 431–438. https://doi.org/10.1007/BF02476705

Keener, J., & Sneyd, J. (Eds.). (2009). The Circulatory System. In *Mathematical Physiology: II: Systems Physiology* (pp. 471–522). Springer. https://doi.org/10.1007/978-0-387-79388-7_1

Koch, T., Schneider, M., Helmig, R., & Jenny, P. (2020). Modeling tissue perfusion in terms of 1d-3d embedded mixed-dimension coupled problems with distributed sources. *Journal of Computational Physics*, *410*, 109370. https://doi.org/10.1016/j.jcp.2020.109370

Kuffner, J., & LaValle, S. (2011). Space-filling trees: A new perspective on incremental search for motion planning, 2199–2206. https://doi.org/10.1109/IROS.2011.6094740

Kundu, P. K., Cohen, I. M., & Dowling, D. R. (2015). *Fluid Mechanics*. Academic Press.

Linninger, A., Hartung, G., Badr, S., & Morley, R. (2019). Mathematical synthesis of the cortical circulation for the whole mouse brain-part I. theory and image integration. *Computers in Biology and Medicine*, *110*, 265–275. https://doi.org/10.1016/j.compbiomed.2019.05.004

Lorthois, S., & Cassot, F. (2010). Fractal analysis of vascular networks: Insights from morphogenesis. *Journal of Theoretical Biology*, *262*(4), 614–633. https://doi.org/10.1016/j.jtbi.2009.10.037

Mandelbrot, B. B. (1977). *The Fractal Geometry of Nature*. W.H. Freeman; Company.

Martino, M. M., Brkic, S., Bovo, E., Burger, M., Schaefer, D. J., Wolff, T., Gürke, L., Briquez, P. S., Larsson, H. M., Gianni-Barrera, R., Hubbell, J. A., & Banfi, A. (2015). Extracellular Matrix and Growth Factor Engineering for Controlled Angiogenesis in Regenerative Medicine. *Frontiers in Bioengineering and Biotechnology*, *3*, 1–8. https://doi.org/https://doi.org/10.3389/fbioe.2015.00045

Masters, B. R. (2004). Fractal Analysis of the Vascular Tree in the Human Retina. *Annual Review of Biomedical Engineering*, *6*(1), 427–452. https://doi.org/10.1146/annurev.bioeng.6.040803.140100

Murray, C. D. (1926). The Physiological Principle of Minimum Work. *Proceedings of the National Academy of Sciences*, *12*(5), 299–304. https://doi.org/10.1073/pnas.12.5.299

Murray, J. D. (Ed.). (2002). *Mathematical Biology: I. An Introduction* (Vol. 17). Springer. https://doi.org/10.1007/b98868

Nordbotten, J. M., & Celia, M. A. (2011). Geological Storage of CO2: Modeling Approaches for Large-Scale Simulation. *Geological Storage of CO 2: Modeling Approaches for Large-Scale Simulation*. https://doi.org/10.1002/9781118137086

Peaceman, D. W. (1978). Interpretation of Well-Block Pressures in Numerical Reservoir Simulation. *SOCIETY OF PETROLEUM ENGINEERS JOURNAL*, 17.

Perdikaris, P., Grinberg, L., & Karniadakis, G. E. (2016). Multiscale modeling and simulation of brain blood flow. *Physics of Fluids*, *28*(2), 021304. https://doi.org/10.1063/1.4941315

Qohar, U. N. A., Zanna Munthe-Kaas, A., Nordbotten, J. M., & Hanson, E. A. (2021). A nonlinear multiscale model for blood circulation in a realistic vascular system. *Royal Society Open Science*, *8*(12), 201949. https://doi.org/10.1098/rsos.201949

Rubin, G., Firlik, A. D., Levy, E. I., Pindzola, R. R., & Yonas, H. (2000). Relationship between Cerebral Blood Flow and Clinical Outcome in Acute Stroke. *Cerebrovascular Diseases*, *10*(4), 298–306. https://doi.org/10.1159/000016074

Schreiner, W., Karch, R., Neumann, M., Neumann, F., Szawlowski, P., & Roedler, S. (2006). Optimized arterial trees supplying hollow organs. *Medical Engineering & Physics*, *28*(5), 416–429. https://doi.org/10.1016/j.medengphy.2005.07.019

Shipley, R., Smith, A., Sweeney, P., Pries, A., & Secomb, T. (2019). A hybrid discrete-continuum approach for modelling microcirculatory blood flow. *Mathematical Medicine and Biology*, *dqz006*, 1–18. https://doi.org/10.1093/imammb/dqz006

Sievers, J. (2022). VoronoiLimit(varargin). https://www.mathworks.com/matlabcentral/fileexchange/34428-voronoilimit-varargin

Sutera, S. P., & Skalak, R. (1993). The History of Poiseuille's Law. *Annual Review of Fluid Mechanics*, *25*(1), 1–20. https://doi.org/10.1146/annurev.fl.25.010193.000245

Talou, G. D. M., Safaei, S., Hunter, P. J., & Blanco, P. J. (2021). Adaptive constrained constructive optimisation for complex vascularisation processes. *Scientific Reports*, *11*(1), 6180. https://doi.org/10.1038/s41598-021-85434-9

Todorov, M. I., Paetzold, J. C., Schoppe, O., Tetteh, G., Shit, S., Efremov, V., Todorov-Völgyi, K., Düring, M., Dichgans, M., Piraud, M., Menze, B., & Ertürk, A. (2020). Machine learning analysis of whole mouse brain vasculature. *Nature methods*, *17*(4), 442–449. https://doi.org/10.1038/s41592-020-0792-1

Troudi, A., Tensaouti, F., Baudou, E., Péran, P., & Laprie, A. (2022). Arterial Spin Labeling Perfusion in Pediatric Brain Tumors: A Review of Techniques, Quality Control, and Quantification. *Cancers*, *14*(19), 4734. https://doi.org/10.3390/cancers14194734

Voß, S., Glaßer, S., Hoffmann, T., Beuing, O., Weigand, S., Jachau, K., Preim, B., Thévenin, D., Janiga, G., & Berg, P. (2016). Fluid-Structure Simulations of a Ruptured Intracranial Aneurysm: Con-

stant versus Patient-Specific Wall Thickness. *Computational and Mathematical Methods in Medicine*, *2016*, 9854539. https://doi.org/10.1155/2016/9854539

Witten, T. A., & Sander, L. M. (1981). Diffusion-Limited Aggregation, a Kinetic Critical Phenomenon. *Physical Review Letters*, *47*(19), 1400–1403. https://doi.org/10.1103/PhysRevLett.47.1400

Zamir, M. (1976). Optimality principles in arterial branching. *Journal of Theoretical Biology*, *62*(1), 227–251. https://doi.org/10.1016/0022-5193(76)90058-8

Zamir, M. (1999). On fractal properties of arterial trees. *Journal of Theoretical Biology*, *197*(4), 517–526. https://doi.org/10.1006/jtbi.1998.0892